A mesh adaptation strategy for complex wall-modeled turbomachinery LES

Nicolas Odier[a,*], Adrien Thacker[b], Maël Harnieh[a], Gabriel Staffelbach[a], Laurent Gicquel[a], Florent Duchaine[a], Nicolás García Rosa[b], Jens-Dominik Müller[c]

[a]*CFD Team, CERFACS, 31057 Toulouse, France*
[b]*Institut Supérieur de l'Aéronautique et de l'Espace, 31055 Toulouse, France*
[c]*Queen Mary University of London, United Kingdom*

Abstract

A mesh adaptation methodology for wall-modeled turbomachinery Large Eddy Simulation (LES) is proposed, simultaneously taking into account two quantities of interest: the average kinetic energy dissipation rate and the normalized wall distance y^+. This strategy is first tested on a highly loaded transonic blade with separated flow, and is compared to wall-resolved LES results, as well as experimental data. The adaptation methodology allows to predict fairly well the boundary layer transition on the suction side and the recirculation bubble of the pressure side. The method is then tested on a real turbofan stage for which it is shown that the general operating point of the computation converges toward the experimental one. Furthermore, comparison of turbulence predictions with hot-wire anemometry show good agreement as soon as a first adaptation is performed, which confirms the efficiency of the proposed adaptation method.

Keywords: wall-modeled Large-Eddy Simulation, mesh adaptation, complex turbomachinery, hot-wire anemometry, turbulence assessement

*Corresponding author
Email address: `nicolas.odier@cerfacs.fr` (Nicolas Odier)

1. Introduction

Numerical flow prediction inside complex geometries is currently performed in industry using Reynolds Averaged Navier-Stokes (RANS) approaches. For turbomachinery flows, these Computational Fluid Dynamics (CFD) models have indeed proven reliable when focusing on global performance characteristics around nominal conditions at affordable computational cost. They however fail to accurately predict unsteady and chaotic features hence other approaches must be considered. In such cases, Large-Eddy Simulations (LES) has become a good candidate if coupled to available computing resources allowing such simulations to be produced in an academic or industrial context, the latter requiring specific wall treatments. Several approaches have been developed along the years to avoid resolving the boundary layer flow. Among these, one retains hybrid RANS/LES models or the Detached-Eddy Simulation approach proposed by Spalart et al. [58]) which solve RANS equations in the boundary layer and LES equations in the outer layer or main flow stream (cf. the review of DES applications given in Spalart [57]). These hybrid approaches have allowed unsteady simulations of complex turbomachinery geometries (Tucker [61, 62]). Wall-modeling is another alternative that avoids resolving the boundary layer dynamics by assuming a logarithmic velocity profile in the boundary layer to evaluate the wall shear. In this approach, using the first off-the-wall LES grid node, the wall shear stress is provided by the model, usually assuming an inviscid, steady, attached, and no adverse pressure gradient flow (Deardorff [17]). Improvements have been proposed, to take into account non-equilibrium effects (Kawai and Larsson [37], Park and Moin [46]), or a pressure gradient (Afzal [2], Duprat et al. [21]). Wall-modeling for LES is still to this day an on-going research topic (Yang et al. [70, 69], Catchirayer et al. [12], Bae et al. [9]), reviews of wall-modeled LES may be found in Piomelli and Balaras [50], Piomelli [49], Larsson et al. [39], Bose and Park [11]. Similar to RANS/LES or DES approaches, wall-modeling techniques have enabled a growing literature devoted to turbomachinery LES, as detailed in reviews by Dufour et al. [20], Gourdain

et *al.* [32], Tucker et *al.* [61, 62, 63]. LES however remains a research tool, although it is expected to take a growing part in industry and in a close future (Larsson and Wang [40], Gourdain et *al.* [32]). Before efficient use, several points need to be considered for full benefit. First, an appropriate numerical scheme is mandatory to advect the flow with low dispersion and dissipation, while remaining computationally affordable. Second, inlet and outlet boundary conditions remain key points to address adequately compressible and unsteady flows as encountered in real turbomachinery flows. In that respect, characteristic treatments (Poinsot and Lele [51]) are recommended and adequate practices are required in an industrial context (Odier et *al.* [44]). To finish, the design of an appropriate mesh is the last critical point especially in the context of industrial applications. However, the mesh must indeed be designed to accurately predict the important features of the flow: i.e shocks, wakes, tip leakage vortices, turbulent regions and boundary layers. All these phenomena indeed dictate losses (Denton [18]) and have to be captured to ensure proper flow prediction (Amone et *al.* [6]). The meshing step of real systems can be particularly delicate when complex flow physics occurs. As a result, both a significant human time and good experience to refine at first hand interesting regions of such flows are required. In that respect, even experienced users are likely to fail especially when dealing with complex and new geometries as usually encountered in a design phase.

To alleviate the inherent difficulties related to this meshing design, solution-adaptative procedures have been proposed to tailor local mesh size and consequently to improve the numerical accuracy of the solution at a given cost. These approaches determine the local mesh size by considering either a solution-based measure or on an error-estimator. Some authors proposed to adapt a given mesh with the objective of minimizing an interpolation error, for example taking the Hessian matrix of any given quantity. Frey and Alauzet [25] or Alauzet et *al.* [3] for example proposed to build a metric matrix allowing to adapt edge lengths. Adjoint-based techniques have also been used as error-estimate (Giles

3

and Pierce [27, 48]) to perfom mesh adaptation (Müller and Giles [42], Venditti and Darmofal [65]). A review of mesh adaptation methodologies is available in Fidkowski and Darmofal [22] showing that such techniques have been successfully employed for the past years in Euler or RANS CFD of external flows (Jones et *al.* [36], Nemec and Aftosmis [43], Peter et *al.* [47]).

Both solution-based and adjoint-based techniques have been applied to turbomachinery configurations. For unstructured, viscous, and compressible CFD, the potential of adapting the mesh using a solution-based approach has been demonstrated by the preliminary work of Dawes [16] in a RANS context. More recently, adjoint-based mesh adaptations for quite complex geometries and for multiblock structured meshes have been performed by Ali et *al.* [5, 4], either focusing on the axial velocity, total pressure losses, or iso-surface of a distance field. In the same line, Frazza et *al.* [24] performed Hessian-based anisotropic mesh adaptation on the NASA rotor 37 (Denton [19]) as well as the high pressure turbine cascade LS89 (Arts et *al.* [8]) configuration focusing on the Mach number field and then latter using a wall-distance sensor for a $2D$ RANS wall-modeled simulation [23]. Similarly, Vivarelli et *al.* [66] proposed both a Hessian-based and an adjoint-based anisotropic mesh adaptation procedure for the NASA rotor 37, to then consider a mesh adaptation strategy based on adjoint quantities only, and considering the total pressure ratio, total temperature ratio, and adiabatic efficiency (Vivarelli et *al.* [67]). Finally, a methodology to adapt a mesh accounting for shocks and vorticity is presented in Gou et *al.* [30] for the rotor 37 configuration specifically targeting the interactions between shock waves, boundary layers and tip leakage flows.

If mesh adaptation has been rapidly introduced to RANS, very few contributions address such techniques for LES and for complex geometries. For structured meshes, Antepara et *al.* [7] proposed parallel mesh refinement based on a multi-scale decomposition theory, while Toosi and Larsson [60] proposed an anisotropic mesh adaptation using a Hessian-based error indicator considering small-scale energy. For unstructured meshes, Benard et *al.* [10] proposed a

4

double criterion ensuring both the mean field prediction and a sufficient LES quality criterion (Pope [52]), similarly to Gou et *al.* [29]. More recently an alternative approach has been proposed by Daviller et *al.* [15] specifically for LES, basing their refinement criterion on the averaged kinetic energy dissipation rate to accurately predict pressure losses in complex geometries.

The present work is a continuation of the last cited publication, aiming at automatically adapting the mesh for wall-modeled, unstructured, complex turbomachinery flows so as to produce accurate LES predictions. This paper is organized as follows: the mesh adaptation methodology is described in section 2. Section 3 describes the application of the approach to a highly loaded blade for which flow separation occurs. The focus is here placed on the accuracy of the predicted average quantities. Comparisons with a wall-resolved LES prediction of the same flow and available experimental results are provided to evaluate the wall-modeled LES technique when coupled to mesh adaptation. Section 4 assesses the strategy on a complex rotor-stator configuration through comparisons with experimental measurements, focus being put on the resulting turbulent characteristic predictions.

2. Mesh adaptation methodology

In their orignial contribution, Daviller et *al.* [15] propose to construct a field of metric evaluated from the mean LES prediction, highlighting the importance of the averaged kinetic energy dissipation rate within the flow. Their criterion enable good prediction of the actual pressure losses in a swirler LES known to be challenging. Their methodology is briefly recalled in the following, the quantity of interest under consideration being the time averaged dissipation rate,

$$\overline{\overline{\tilde{\Phi}}} = \overline{(\mu + \mu_t) \left(\frac{\partial \tilde{u}_i}{\partial x_j} + \frac{\partial \tilde{u}_j}{\partial x_i} \right)^2}, \tag{1}$$

where μ is the laminar viscosity, μ_t the Sub-Grid Scale (SGS) turbulent viscosity, $\tilde{u}$ the LES filtered velocity field, and $\overline{}$ is the temporal averaging operator.

Based on Eq. (1), the following non-dimensional metric is proposed,

$$\Phi^\star = \left[1 - \left(\frac{\overline{\overline{\Phi}} - \overline{\overline{\Phi}}_{min}}{\overline{\overline{\Phi}}_{max} - \overline{\overline{\Phi}}_{min}} \right) \right]^\alpha, \quad \Phi^\star \in [0:1], \tag{2}$$

where α is a magnifying factor allowing to smooth singularities, to be adapted depending on the configuration under study, while the subscripts $_{min}$ & $_{max}$ are respectively the maximum and minimum values reached in the predicted field of $\overline{\overline{\Phi}}$. Finally, this metric is used as an edge size multiplicating factor augmented by a minimum parameter, ϵ to avoid very small cells, so that:

$$\text{metric} = \Phi^\star(1 - \epsilon) + \epsilon. \tag{3}$$

With such definitions, and using wall-resolved simulations, the authors showed that two adaptation steps are enough to predict actual pressure losses in a swirler with less than 1% error. As stated in the introduction, losses are a key parameter in turbomachinery since they impose the resulting mass-flow rate and the machine efficiency as soon as the pressure ratio is enforced between an inlet and an outlet. For wall-modeled simulations, the normalized wall distance y^+ is a clear quantity of interest to be carefully considered. Indeed, the wall-law accurately predicts the wall-shear stress only if the first off-the-wall grid nodes are within a range of values usually dependent on the model implementation and numerics used. Since losses occuring out of the boundary layer are influenced by the boundary layer prediction, and vice-versa, the methodology proposed in the present paper consists in simultaneously accounting for both quantities of interest. To do so, a double criterion definition is proposed so that,

$$\begin{cases} \text{metric}_{wall} = \frac{y^+_{target}}{y^+} & \text{for all cells on a wall} \\ \text{metric}_{flow} = \Phi^\star(1 - \epsilon) + \epsilon & \text{for all other cells} \end{cases} \tag{4}$$

where $\Phi^\star$ is the formulation proposed by Daviller et al. [15] and expressed by Eq. (2). In the present paper a linear relation $u^+ = y^+$ is considered if $y^+ < 11$, and $u^+ = \kappa^{-1} ln \left(A \frac{y u_\tau}{\nu} \right)$ is assumed otherwise, with $A = 9.2$, $\kappa = 0.41$, ν the kinematic viscosity and $u_\tau = \sqrt{\frac{\tau_{wall}}{\rho}}$. The target normalized wall distance for

6

the first off-the-wall grid node is set at $y^+_{target} = 30$. Once obtained the metric field is then used as a refinement factor to adapt the mesh using the MMG3D library [14]. Note that for the present paper, all simulations are performed using the LES code AVBP, an explicit unstructured massively parallel solver detailed in Schønfeld et al. [55] and Gourdain et al. [31]. This solver allows several numerical schemes: the Lax-Wendroff [41] finite-volume 2nd order in space and time, as well as a two-step Taylor-Galerkin finite-element scheme (Colin and Rudgyard [13]) specifically designed for LES on unstructured grids and which is 3rd order accurate in space and time.

3. Flow prediction around a High Pressure turbine blade with flow separation

Although necessary for real industrial flows, the use of a logarithmic law-of-the-wall in turbomachinery LES introduces a major approximation. Indeed, such a model is intended for a fully established and attached flow over a flat plate. These assumptions are believed to be verified in turbomachinery configurations, where an unsteady flow occurs over curved surfaces thus inducing pressure gradients, with flow transitioning from a laminar to a turbulent regime, and with potential detachments. Such models remain nonetheless mandatory since the cost of performing a wall-resolved LES of such a configuration is still computationally intractable for industry [32]. To evaluate the law-of-the-wall performance for a realistic configuration, the above described methodology is first tested on the high pressure turbine blade T120 (Gomes and Niehuis [28]), characterized by a significant blade curvature leading to the presence of a re-circulation bubble on the pressure side. On the suction side, a transition to turbulence is also present induced by a sonic shock in the inner blade channel. The accurate prediction of this flow is particularly challenging and inlet turbulence is seen to significantly affect the generation of the re-circulation bubble on the pressure side impacting the average pressure distribution within the inner vane passage (Harnieh et al. [34]). In this current section 3, successive mesh-

adaptations are engaged for a wall-modeled LES to evaluate the proposed strategy to address this challenging flow in a wall-modeled context. This test-case furthermore offers a good context of validation since a wall-resolved simulation exists, as well as experimental measurements. Note that the wall-resolved prediction has been obtained using a user-defined and hand made mesh. In that case, a meshing effort is made inside the blade passage, the wake, as well as between the inlet and the leading edge, to convect properly the injected turbulence. Results are available in Harnieh et al. [33, 34], showing very good agreement with experimental measures. They are therefore a relevant reference to gauge the effect of wall modeling for such flows. The general flow topology obtained on this user-defined wall-resolved mesh is presented in Fig.1, where a contour of unitary Mach number $M = 1$ is plotted in white, and a contour of zero axial velocity is plotted in black. This instantaneous view evidences on the suction side, a shock between the blade and the surrounding wake, while on the pressure side, a recirculation bubble appears due to the blade strong curvature.
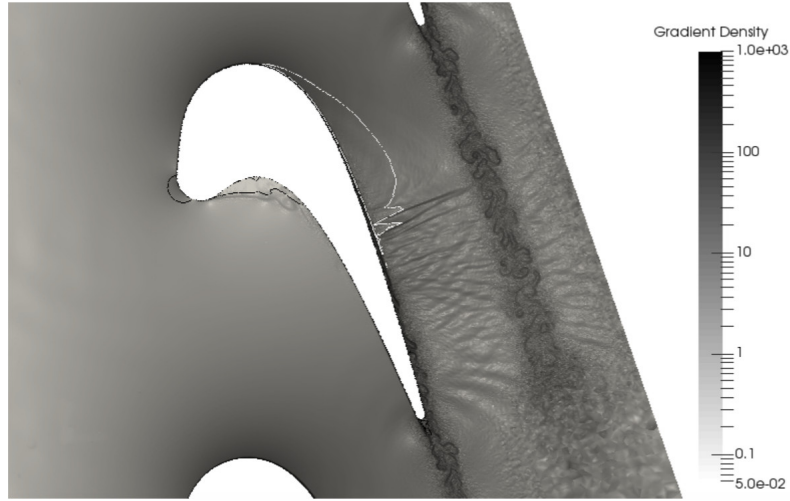
Figure 1: General flow topology: Instantaneous field of density gradient. Contour of $M = 1$ is plotted in white, contour of null axial velocity is plotted in black.

In order to evaluate the proposed mesh adaptation methodology, a first simulation is performed on a coarse mesh, using a Lax-Wendroff scheme, 2nd order in space and time, to establish the general flow topology. Just like in Harnieh et al. [33], synthetic turbulence is injected at the inlet, using the same turbulence characteristics that were shown to match the experimental measurements close to the leading edge. Based on the resulting average predicted quantities, a metric is built using Eq.4, and a first mesh adaptation is performed leading to an adapted mesh named "AD1". The initial solution of mesh "AD1" is interpolated from an instantaneous flow realization on the original coarse mesh. Then and for subsequent simulations, the TTGC numerical scheme, 3rd order in space and time (Colin and Rudgyard [13]), is selected to obtain first a new prediction on the basis of the adapted mesh "AD1". Note that, a second mesh adaptation is then performed using the average flow quantities obtained on "AD1" to yield a new mesh named "AD2", on which the simulation is again performed.

The successive fields of metric used to perform the two successive adaptations are presented in Fig.2, showing both the flow domain and the wall. Note that red regions correspond to regions that need refinement. The first mesh adaptation requires some refinement close to the inlet, where dissipation occurs due to the injected turbulence, as shown in Fig. 2(a). A large region over the suction side and within the inner blade channel is also to be refined, as well as the recirculation zone of the pressure side, and areas within the wake. Most of the wall mesh is also identified as needing refinement, to reach the target y^+, as seen in Fig. 2(c). Turning our attention to the second adaptation step, the mesh also requires refinement on the suction side and in the channel, within the wake, as well as in the recirculation zone on the pressure side (Fig. 2(b)). Wall refinement is also needed for this second adaptation step, as shown in Fig. 2(d), but a more reasonnable effort if compared to the first adaptation. The two adapted meshes are presented along with views of the user defined wall resolved mesh in Figs 3, with a focus on the leading edge and the trailing edge areas. Consistent with the maps of the metric, refinement is applied close to the suction side,

| Case	Total cells number	Time Step	hCPU/ convective time
Coarse	0.7 million	5.2e-7 s	4.5
Adapt1	3.5 millions	7.8e-8 s	270
Adapt2	42.4 millions	2.7e-8 s	8340
Resolved	33.8 millions	2.1e-8 s	14060

Table 1: Meshes and computational details for T120 configurations

within the inner vane channel, in the re-circulation bubble zone on the pressure side, around the blade wall and within its wake. Note that cell distributions in adapted meshes is smoother and more accurately distributed than in the reference user-defined mesh.

Mesh characteristics and corresponding computational costs are summarized in Table 1. Note that "AD2" is composed of more cells than the used-defined resolved mesh, due to the wake refinement that hasn't been considered in the resolved mesh. Prisms used in this last mesh to resolve the boundary layers however induce a small time-step, resulting in a higher computational cost than with "AD2".

3.2. Comparison between wall-resolved and adapted wall-modeled results

The distribution of average losses of kinetic energy (LIKE) issued by the wall-resolved LES, the coarse wall-modeled LES and the two adapted mesh predictions are presented in Fig. 4. As observed in Fig. 4(a) for the wall-resolved solution, the map of LIKE mainly evidences dissipation in the suction side boundary layer and within the wake. Overall, all wall modeled based predictions evidence the same characteristics. Levels of dissipation reached by the coarse mesh are however excessive in the strongly accelerating flow suction side region (Fig. 4(b)). Similarly, the shock region on the suction side, as well as the blade boundary layer are excessively marked if compared to the wall-resolved field. The main consequence of the adaptation process (Figs. 4(c) and 4(d)) is to produce LIKE fields that are clearly in a better agreement with the reference

10
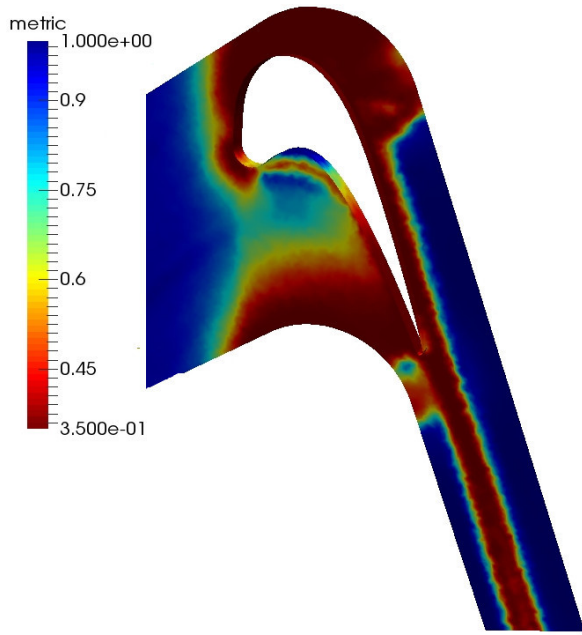
(a) Map of metric to perform the first mesh adaptation.
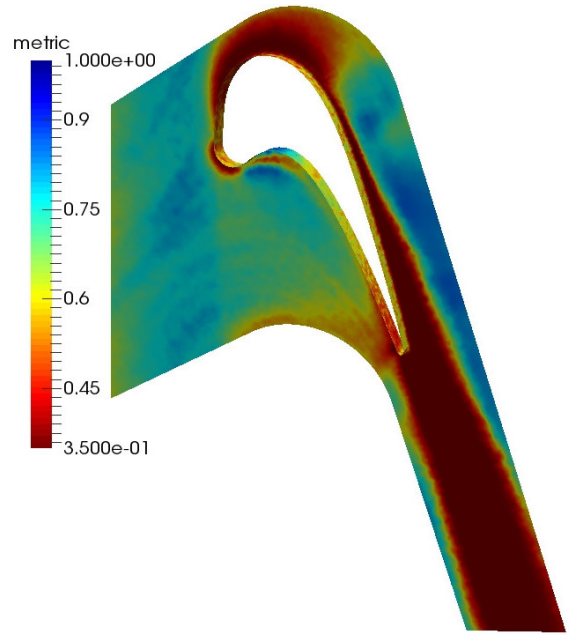
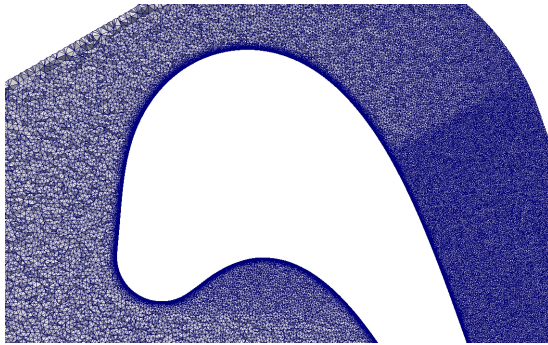(b) Map of metric to perform the second mesh adaptation.
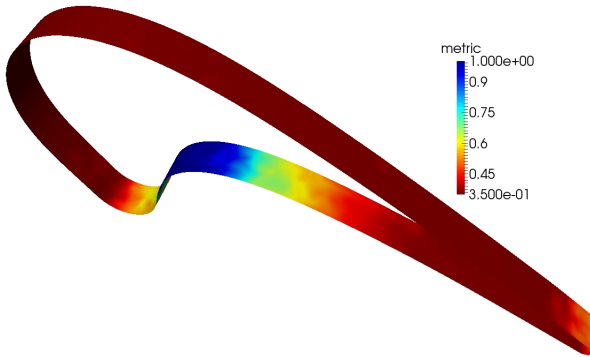
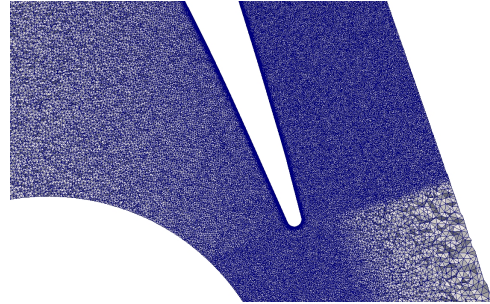(c) Wall metric to perform the first mesh adaptation.
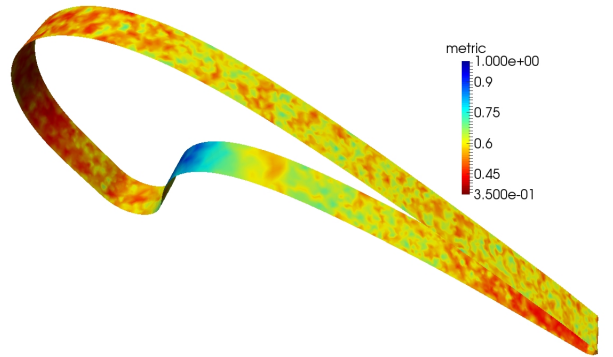
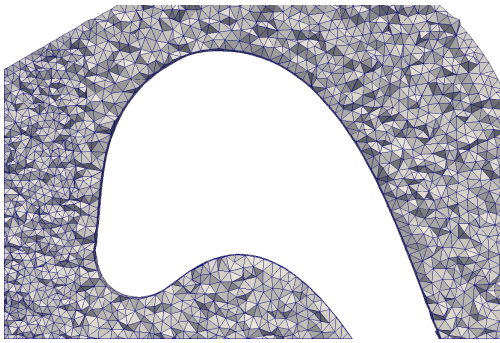(d) Wall metric to perform the second mesh adaptation.

Figure 2: Resulting metrics to perform the two successive mesh adaptations.
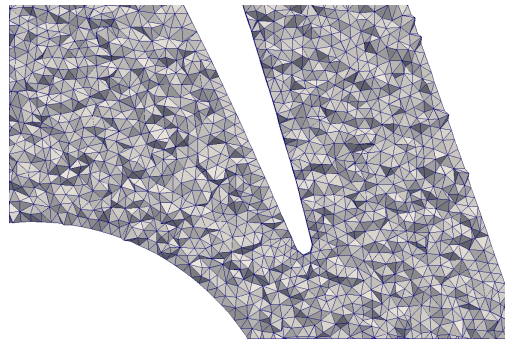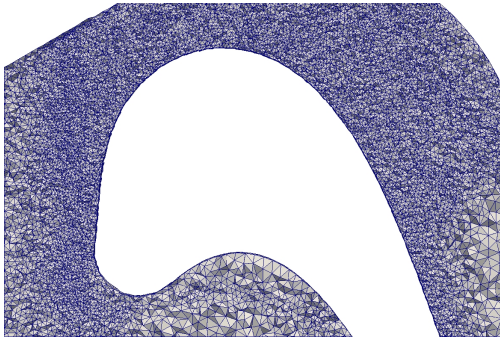
(a) User-defined wall resolved mesh.
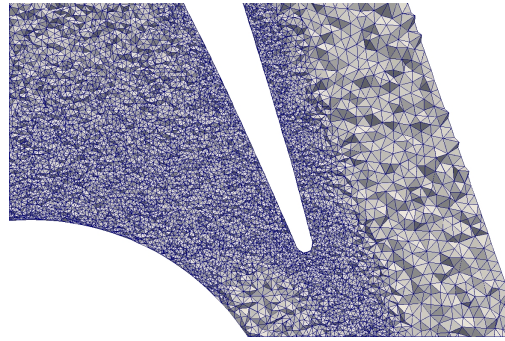
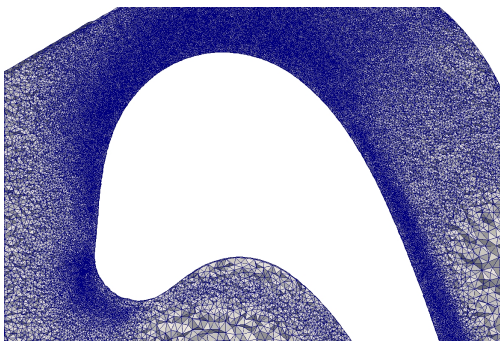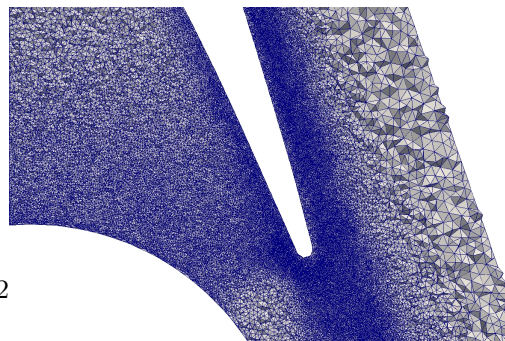(b) User-defined wall resolved mesh.

(c) Coarse mesh.

(d) Coarse mesh

(e) First adaptation "AD1".

(f) First adaptation "AD1".

(g) Second adaptation "AD2".

(h) Second adaptation "AD2".

Figure 3: Meshes comparison: zoom on leading edge.

simulation. The losses associated to the shock on suction side attenuates, both suction side boundary layers and the wake producing fields topology and levels that are closer to the wall-resolved results.

Figure 5 depicts a similar comparison for the second quantity of interest, i.e. the average normalized wall distance y^+. By construction, unitary values are found using the wall-resolved mesh, the highest values being reached close the leading edge (Fig.5(a)). Using a wall-modeled formalism along with the coarse mesh yields large values: up to $y^+ = 240$ (Fig.5(b)). These values are significantly reduced to become closer to the target $y^+ = 30$ as soon as the first mesh adaptation is performed, although higher values are still noticeable at the leading and trailing edges (Fig. 5(c)). It is only with the second mesh adaptation that values close to the target are achieved (Fig.5(d)).

Figure 6 is dedicated to the comparison of the average Mach number, where a contour of the sonic line is added in black. As previously discussed, the coarse mesh leads to a strong shock which diminishes as soon as the mesh is adapted, to finish with a reasonable agreement with the wall-resolved results using "AD2". Turning our attention to the wake, it can be also evidenced that the successive mesh adaptations lead to a thinner wake, to finish closer to the wall-resolved results.

As discussed in the introduction, the prediction of a detached recirculating flow is very challenging for a wall-modeled context. Focusing on this specific feature, the evolution of the recirculation bubble with mesh adaptation is shown in Fig. 7(a) to 7(c), in comparison to the wall-resolved prediction (Fig. 7(d)). Despite the use of the wall-law, a fair prediction of the recirculation bubble size is achieved when compared to the wall-resolved prediction.

Although previous analyses confirm the adequacy of the proposed strategy, more quantitative results are detailed hereafter by comparing obtained predictions to available experimental data. First, the resulting average isentropic Mach number around the blade is presented in Fig. 8. As already seen in Fig. 6(a) for example, the flow prediction on the coarse mesh is very inaccurate on the
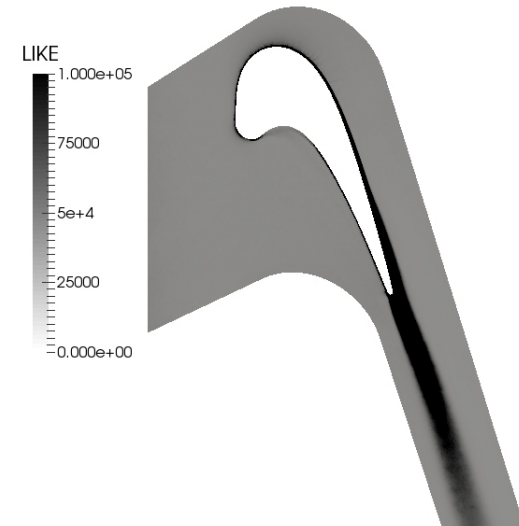
13
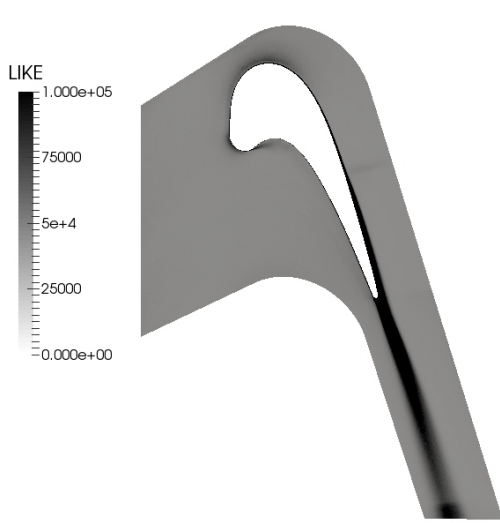
(a) Average kinetic energy dissipation using the wall re-solved mesh.
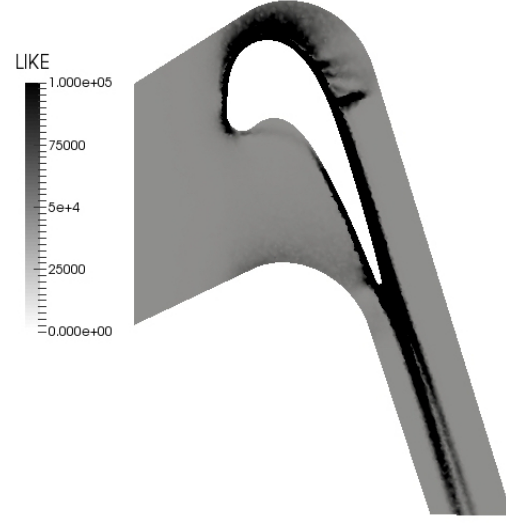
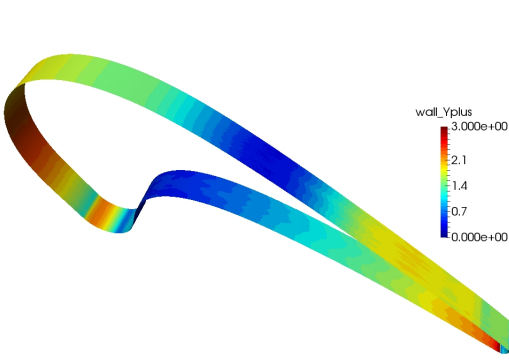(b) Average kinetic energy dissipation on the coarse mesh.
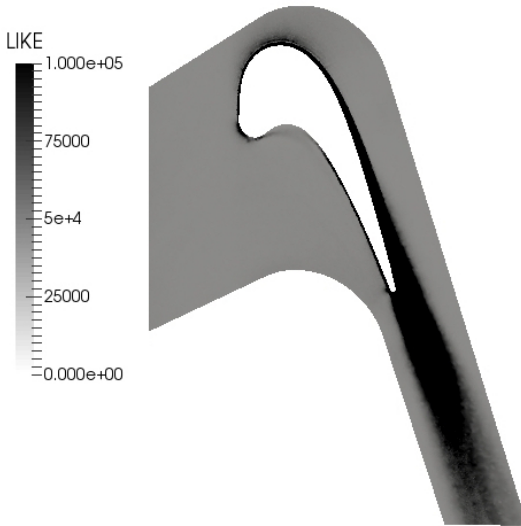
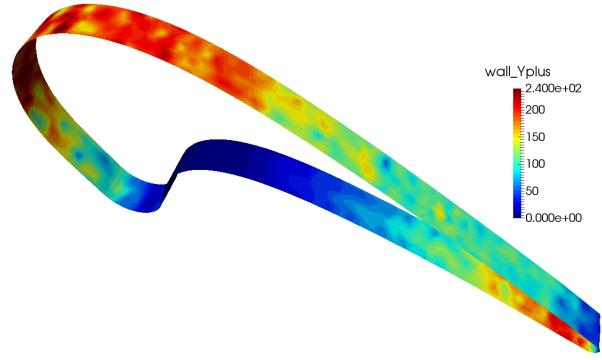(c) Average kinetic energy dissipation using "AD1".
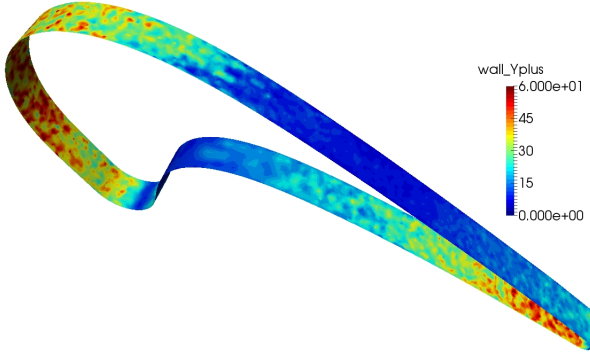
(d) Average kinetic energy dissipation using "AD2".

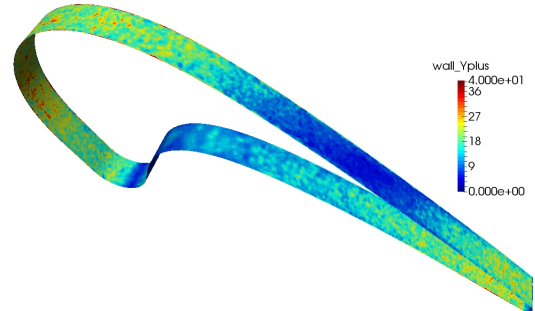Figure 4: Average kinetic energy dissipation on successive meshes.

14

(a) Average wall-distance y^+ using the wall resolved mesh.

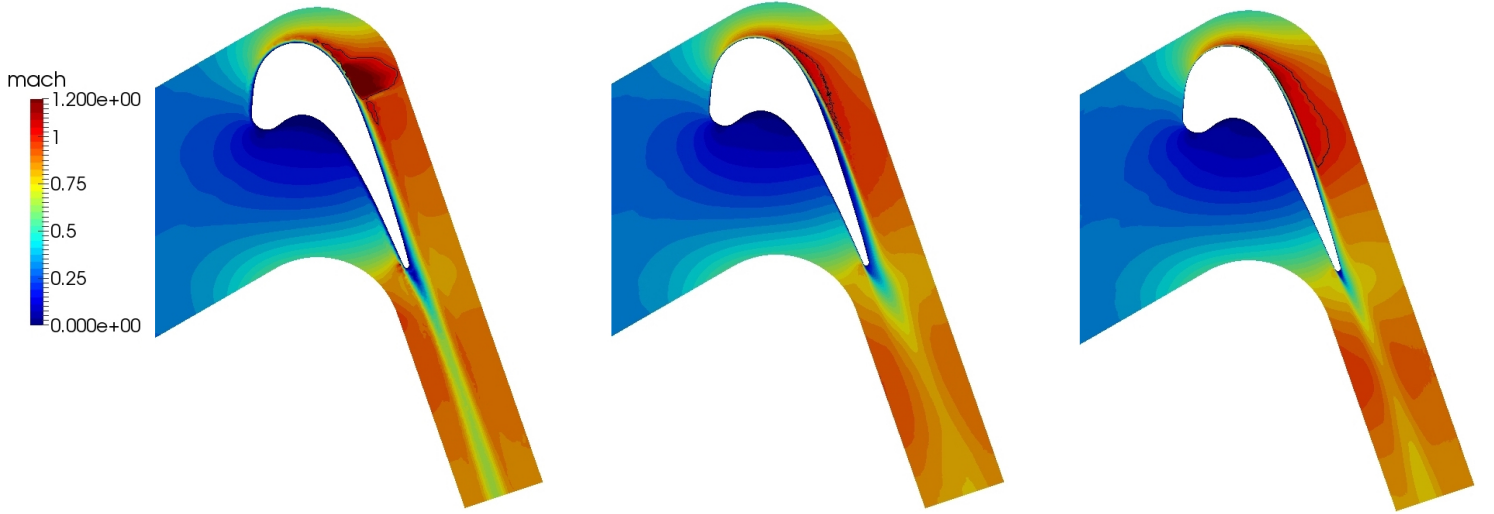(b) Average wall-distance y^+ on the coarse mesh.

(c) Average wall-distance y^+ using "AD1".

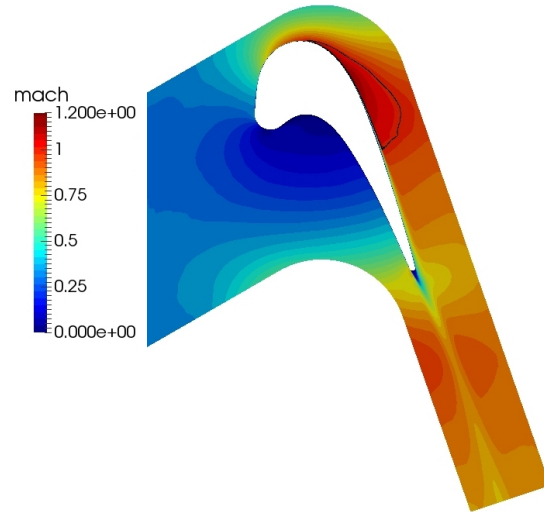(d) Average wall-distance y^+ using "AD2".

Figure 5: Normalized wall distance y^+ on successive meshes.

15

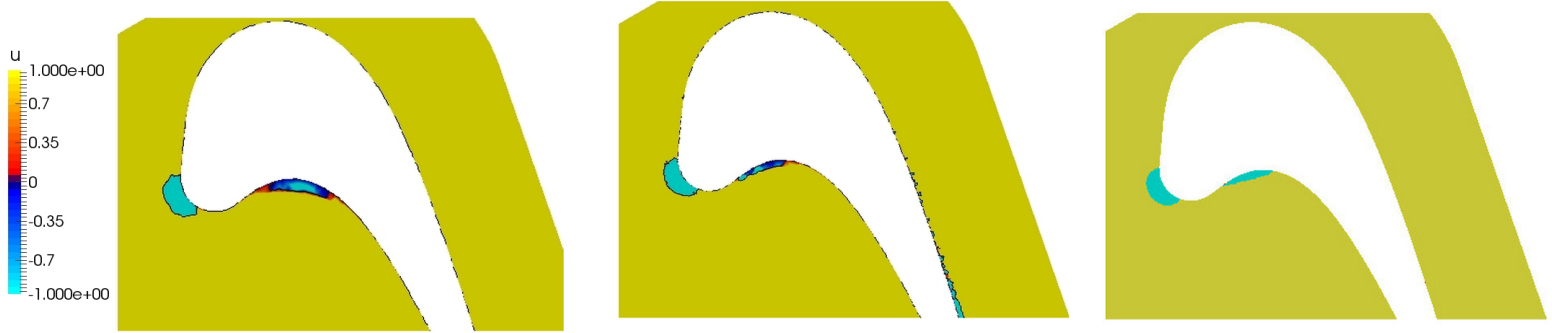(a) Average Mach number using the coarse mesh.

(b) Average Mach number using "AD1".

(c) Average Mach number using "AD2".

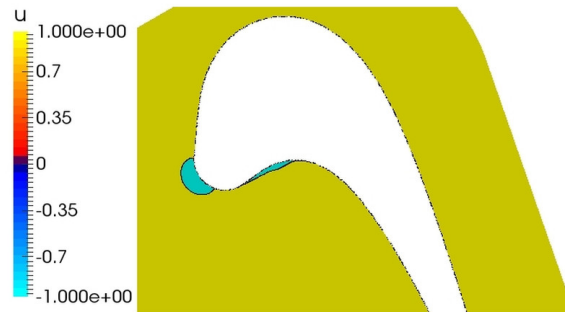(d) Average Mach number using the wall-resolved mesh.

Figure 6: Average Mach numbers along the adaptation steps, and comparison with a wall-resolved simulation. Contour of $M = 1$ is plotted in black.

(a) Recirculation zone using coarse mesh.

(b) Recirculation zone using "AD1".

(c) Recirculation zone using "AD2".

(d) Recirculation zone using a wall-resolved mesh.

Figure 7: Recirculation zone along with mesh adaptation steps.

suction side downstream of the strong blade curvature region. Use of "AD1" improves significantly this part of the flow, without however predicting the shock region on this suction side. "AD2" allows this prediction, even if its location does not match the experimental one. The wall-resolved result is compared to "AD2" and to the experiment in Fig. 8(b) for the sake of clarity. Despite this issue previously discussed on the suction side, a very fair agreement with the experiment is found on the pressure side, where a recirculation bubble takes place.
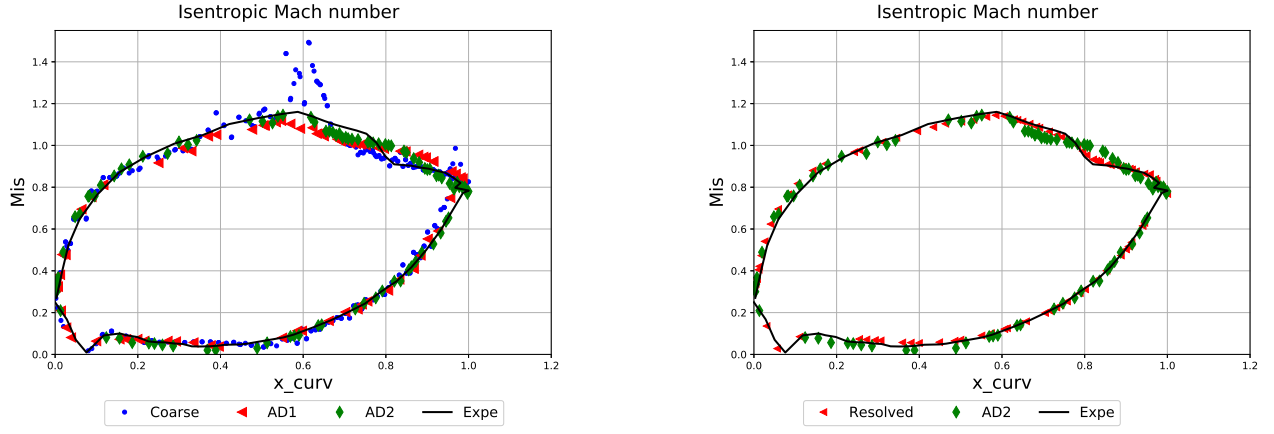
(a) Resulting isentropic Mach numbers along the adaptation steps.

(b) Comparison with wall-resolved simulation.

Figure 8: Resulting isentropic mach numbers.

Figure 9 compares the loss coefficient profile for all configurations in a plane located at $x/c = 0.4$ from the trailing edge, where c is the blade chord. The loss coefficient ξ is defined by Eq. 5:

$$\xi = \frac{P_{t_{LE}} - P_{t_2}}{P_{t_1} - P_2} \tag{5}$$

where $P_{t_{LE}}$ is the total pressure at the leading edge, P_{t_2} is the temporal averaged total pressure measured at $x/c = 0.4$, while P_{t_1} the inlet total pressure and P_2 is the spatial and temporal averaged static pressure at $x/c = 0.4$. Complementary

18

to Fig. 6, this diagnostic shows that the proposed mesh adaptation strategy clearly improves the wake deficit prediction in this wall-modeled context.
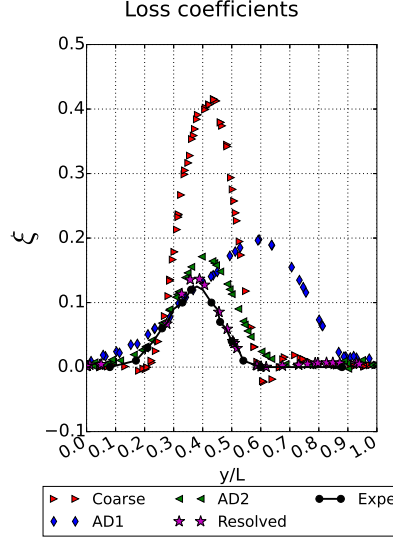

Figure 9: Loss coefficients profiles with adaptation steps

4. Real turbofan configuration:

Section 3 was devoted to the flow prediction of a highly-loaded turbine blade with flow separation, as well as shock region. In the present section, the proposed methodology is evaluated in the case of a real turbofan stage, with focus on the flow unsteady characteristics. The configuration under study is the DGEN-380, a small turbofan designed by Price Induction for personal light jets. This engine has a bypass ratio of 6 and is designed for a cruise Mach number of 0.34 and a thrust of 2.5 kN. Only the fan stage is addressed hereafter. It is composed of 14 rotor blades and 40 stator vanes, for a 1.2 total pressure ratio at maximum power.

19

4.1. Experimental configuration

Measurements have been performed at the DGEN-380 test facility of ISAE-Supaero, depicted in Fig. 10, showing stations 2A, 2RD, 21A which are of interest in the present study. The operating point is assessed by using conventional pressure and temperature measurements. Time averaged profiles of total temperature, total pressure and Mach number are obtained using a five hole probe including a K-type temperature probe. Note that intrusion ports have been specifically designed to enable azimuthal displacement, allowing a 9°angular sector investigation at stations 2RD and 21A. Hot-wire measurements complement this set of data using a Dantec 2D fiber-film probe 55R52 shown in Fig 11, allowing the unsteady measurement of $u_x(\mathbf{x}, t)$ and $u_\theta(\mathbf{x}, t)$, respectively the axial and azimuthal velocity components. In that case, the hot-wire sampling frequency is 300 kHz and measurements are performed over 700 rotations. The experimental measurement grid for hot-wire anemometry is shown in Fig 11 for stations 2RD and 21A. A homogeneous measurement grid is chosen at station 2RD downstream of the rotor, while a refined grid is considered in the stator wake region at station 21A. The experimental constraints associated to measurement duration allow the characterization of one station per day. Consequently, pressure, temperature, mass flow and fan rotational speed have been standardized according to the atmospheric pressure and temperature during each measurement campaign using Eqs. (6), where Pref = 101325 Pa and Tref = 288.15 K. More details about the experimental measurements may be found in García Rosa et al. [26] and in Thacker et al. [59]. Finally, the considered operating point is $N_{std} = 11460\ rpm$, corresponding to 85% of the maximum power, leading to $Q_{std} = 12.1\ kg/s$ and a total pressure ratio of $\Pi_t = 1.14$ between stations 2A and 21A.

$$P_{std} = P\frac{P_{ref}}{P_{atm}}, \quad T_{std} = T\frac{T_{ref}}{T_{atm}}, \quad Q_{std} = Q\sqrt{\frac{T_{atm}}{T_{ref}}}\frac{P_{ref}}{P_{atm}}, \quad N_{std} = N\sqrt{\frac{T_{ref}}{T_{atm}}}$$
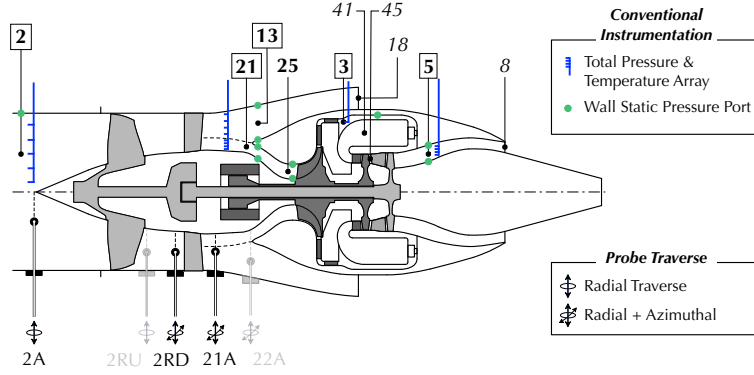
$$(6)$$

20

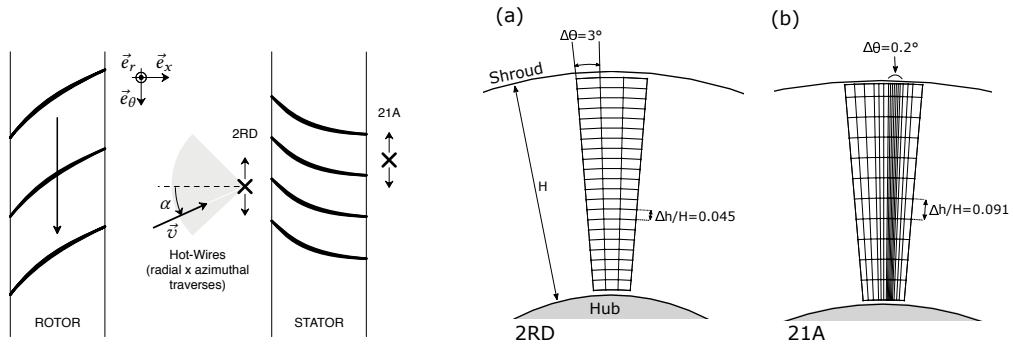Figure 10: DGEN-380 instrumentation. Location of positions 2A, 2RD, and 21A.

Figure 11: Dantec 2D probe 55R52 (left), and experimental grid measurement at stations 2RD (a) and (21A) (b).

21

4.2. Numerical configuration

The numerical approach chosen to handle the rotor-stator interface relies on the MISCOG methodology detailed in Wang et al. [68] and de Laborderie et al. [38]. This approach consists in coupling two LES simulations, one in the rotating domain, the other in the static domain. These two single LES are here performed using AVBP previously described in section 2. At the inlet, a characteristic boundary condition (Poinsot and Lele [51]) imposes total pressure, total temperature, as well as flow direction through the non-reflecting formalism detailed in Odier et al. [45]. Since the experimentally measured turbulence is less than 1% at the inlet, no turbulence is injected in the simulation. At the outlet, a characteristic formulation imposes a static pressure, which is manually fixed by the user to recover the experimental total pressure at station 21A. To alleviate the computational cost, the real geometry has been modified to simulate 42 stator vanes instead of 40, thus allowing the simulation of a 360/14 periodic sector, with 1 rotor blade and 3 stator vanes. Note that a scaling factor has been applied to the stator vanes to keep the original solidity of the real geometry, as suggested in Rai and Madavan [53]. The numerical domain used for the simulations to be detailed hereafter is shown in Fig 12, depicting the inlet and the outlet boundary positions, together with the three measurement stations, 2A, 2RD, and 21A.
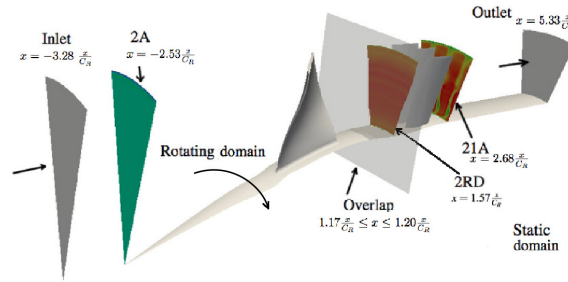

Figure 12: Numerical configuration: boundary locations and experimental measurement stations, where C_R is the rotor chord at midspan.

4.3. Metric and successively adapted meshes

The same methodology as described for the T120 blade of Section 3 is followed here to result in two successive mesh adaptations and three predictions. Similarly to the previous case, a first simulation is carried out with a coarse mesh using a Lax-Wendroff numerical scheme. The average flow resulting from this coarse mesh simulation gives rise to a field of metric according to Eq. 4, which leads to a first adapted mesh "AD1". On this adapted mesh, a second simulation is performed using a two-step Taylor-Galerkin numerical scheme (Colin and Rudgyard [13]), 3rd order in space, 4th order in time. The mesh adaptation is then repeated to get a last "AD2" adapted mesh. The fields of metric leading to the first adapted mesh "AD1" and the second one "AD2" are respectively shown in Fig 13 and 14 for the rotor domain. In both cases, the blade wall is colored by the obtained metric and two axial planes, respectively at $x = -0.01\frac{x}{C_R}$ and $x = 0.05\frac{x}{C_R}$ to illustrate the corresponding adapted mesh in the volume. Note that red fields correspond to regions with small metric values, inducing a local mesh refinement. For the first adaptation (Fig. 13) a noticeable refinement all along the leading edge of the rotor blade appears along with a significant cell count inside the tip vortex region and in the wake region. Note that even an experienced user would have had difficulties to a priori refine these exact regions of interest. Turning our attention to the field of metric leading to the second final mesh "AD2", it can be noticed from Fig. 14 that the same flow features are identified: leading edge, wake, and tip-leakage finer regions. The rotor blade surface is however less refined than in the first adaptation since y^+ values have already reached values close to the target, i.e $y^+ = 30$.

A zoom on the tip-gap region at $x = -0.01\frac{x}{C_R}$ is provided in Fig. 15 to illustrate the impact of the grid refinement in this specific region. The first adaptation induces a mesh refinement on the pressure side, inside the tip gap, on the shroud, and also in a region between the suction side and the tip-leakage flow, corresponding to an entrainment of the flow induced by the tip-leakage and the rotating motion. Note that these regions are refined once again with the second adaptation. However, the entrainement region has moved towards
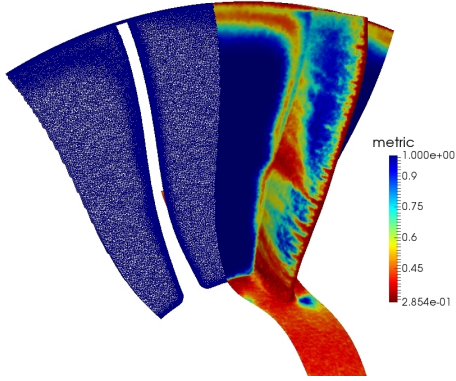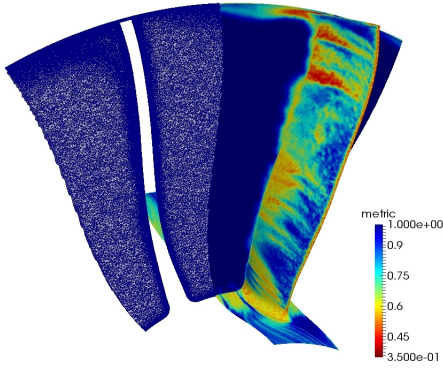
23

(a) Rotor blade and axial cut at $x = -0.01\frac{x}{C_R}$, colored by the field of metric leading to "AD1". The corresponding adapted mesh is also depicted.
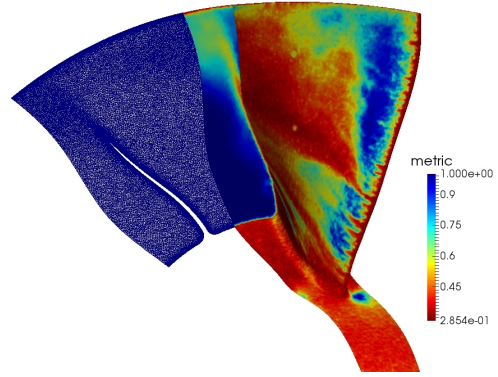
(b) Rotor blade and axial cut at $x = 0.05\frac{x}{C_R}$, colored by the field of metric leading to "AD1". The corresponding adapted mesh is also depicted.

Figure 13: Field of metric leading to the first adapted mesh "AD1" (right), and corresponding adapted mesh "AD1" (left).

(a) Rotor blade and axial cut at $x = -0.01\frac{x}{C_R}$, colored by the field of metric leading to "AD2". The corresponding adapted mesh is also depicted.
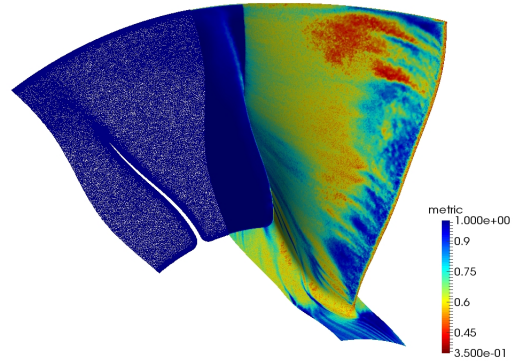
(b) Rotor blade and axial cut at $x = 0.05\frac{x}{C_R}$, colored by the field of metric leading to "AD2". The corresponding adapted mesh is also depicted.

Figure 14: Field of metric leading to the second adapted mesh "AD2" (right), and corresponding adapted mesh "AD2" (left).

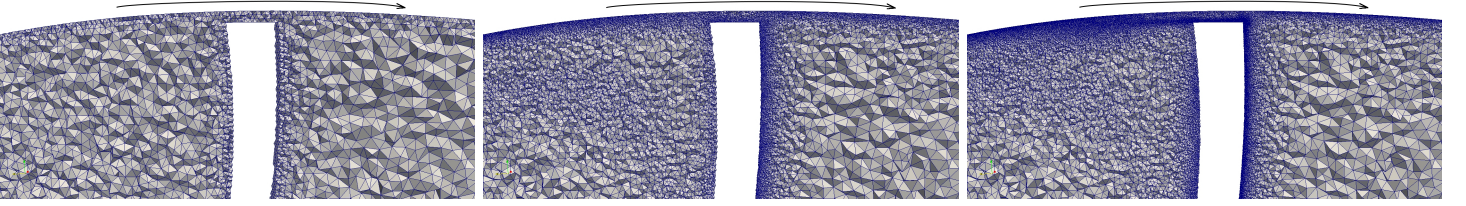the shroud and a clear mixing region due to the tip leakage appears.

Figure 15: Zoom on tip gap region. Coarse mesh (left), "AD1" (center), "AD2" (right).

Similar views to Fig. 15 but focusing on the rotor leading edge at 60% height is provided in Fig. 16. Leading edge refinement appears immediately with the first adaptation, accompanied by a rather large refined region on the suction side near wall. The second adaptation enhances the leading edge refinement, which relaxes within the suction side boundary layer.
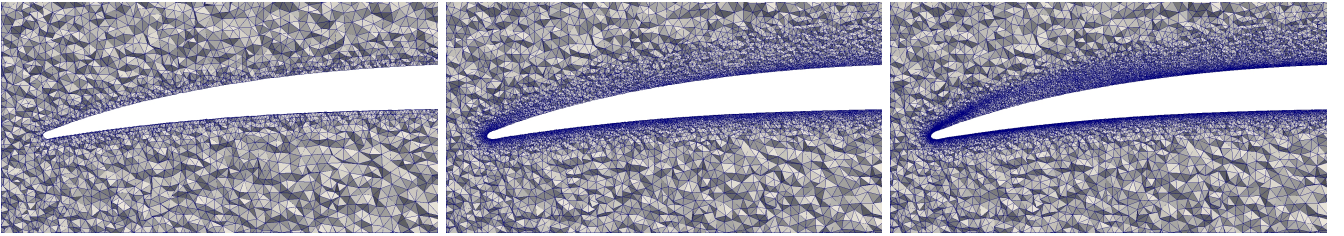
Figure 16: Zoom on rotor leading edge at h/H=60%. Coarse mesh (left), "AD1" (center), "AD2" (right)

For the stator domain, the respective fields of metric for the first and the second mesh adaptations are shown in Fig 17 for the vane and for an axial plane located at $x = 2.533 \frac{x}{C_R}$, i.e. in the stator wake region. For both adaptations and on the vane suction side, a large region is refined close to the leading edge. The first evaluated metric (Fig. 17(a)) enhances grid refinement in the corner vortices present on both hub and shroud, the stator wake region, and more generally the hub and shroud vicinities. The second adaptation (Fig. 17(b)) also refines the

25

wake and the hub corner vortex, but in a smaller proportion than for the first mesh adaptation. A significant refinement around the stator leading edge still appears in this second step, while only few refinement is necessary in the stator wake region and for the shroud vortex corner.

(a) Stator vane and axial cut at $x = 2.533 \frac{x}{C_R}$, colored by the field of metric leading to "AD1" (left). The corresponding adapted mesh is also depicted (right).

(b) Stator vane and axial cut at $x = 2.533 \frac{x}{C_R}$, colored by the field of metric leading to "AD2" (left). The corresponding adapted mesh is also depicted (right).

Figure 17: Stator domain: Field of metric leading to the second adapted mesh "AD2" (left) and corresponding adapted mesh (right).

An iso-span view of the meshes is shown in Fig 18 ($h/H = 0.95$), i.e. focus of the shroud corner vortex. In that case, the entire pressure side is refined with "AD1", together with the leading edge vicinity on the suction side. The domain corresponding to the corner vortex region on the suction side is also refined, but with less intensity than the leading edge region. Finally, the wake is refined, and the same features can be pointed out for the second adaptation. A zoom on the stator leading edge, Fig 19, provides more insight on the second adaptation. Indeed, it evidences both leading edge refinement, as well as a suction side and pressure side refinements.

The mesh characteristics and computational costs associated to these adaptation processes are sumarized in Table 2, underlining a significant computational cost for the second adaptation, particularly due to the small time-step.

26

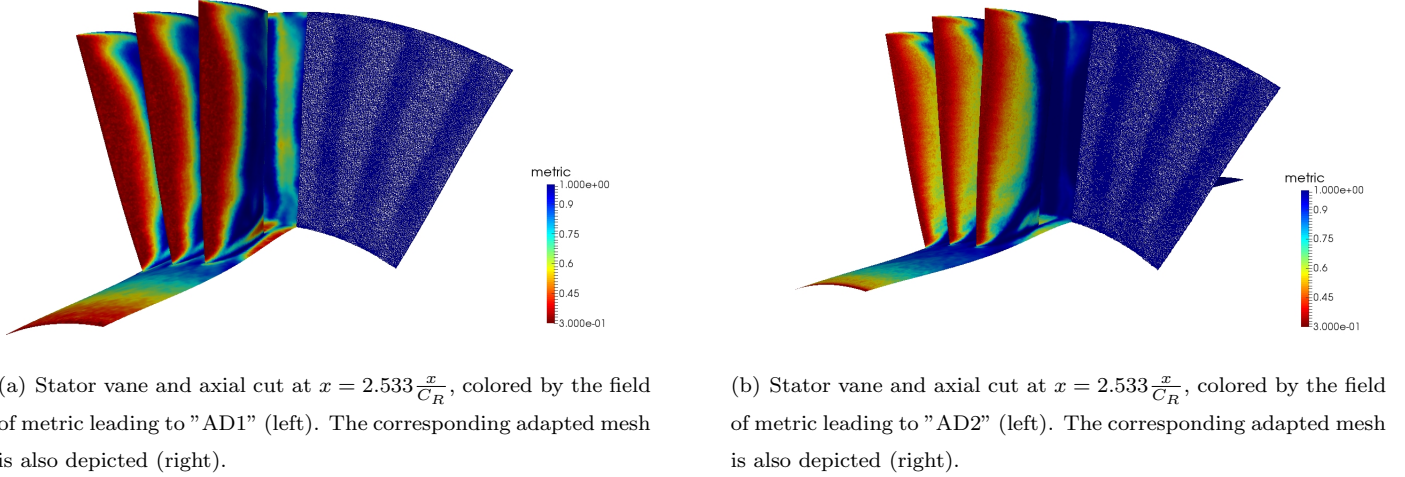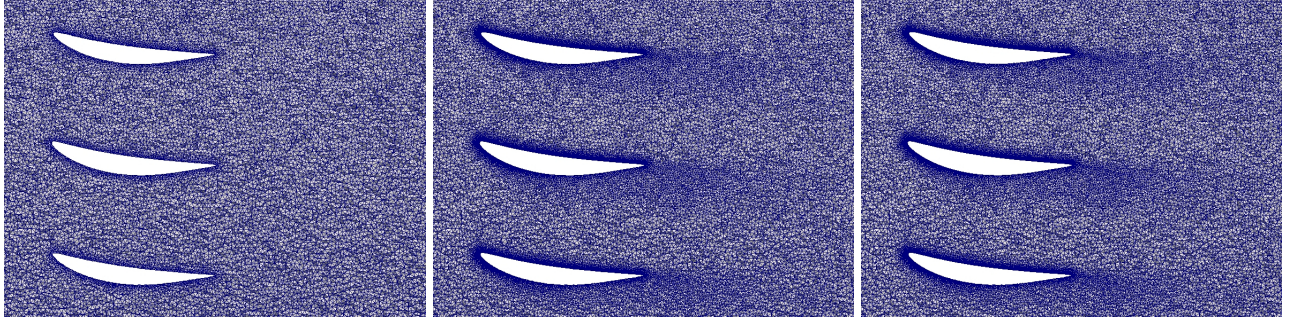Figure 18: Stator: Radial cut at h/H=95%. Coarse mesh (left), "AD1" (center), "AD2" (right)
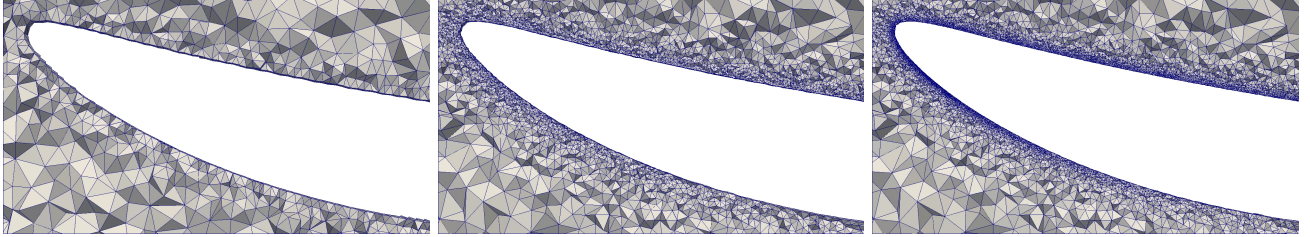
Figure 19: Stator: Radial cut at h/H=95%. Zoom on Stator Leading Edge. Coarse mesh (left), "AD1" (center), "AD2" (right)

Case	Total cells number	TimeStep	hCPU/ rotation
Coarse	47.3 millions	7e-8 s	3510
Adapt1	162.7 millions	1.4e-8 s	155000
Adapt2	350.0 millions	0.48e-8 s	1040000

Table 2: Meshes and computational details for the DGEN configuration

27

4.4. Flow predictions as a result of the mesh adaptation

The evolution of flow predictions can first be analysed by investigation of the numerical operating point resulting from each adaptation, as shown in Fig 20. For each case, the mass-flow, total pressure ratio between station 2A and 21A, and the outlet static pressure evolutions are provided as a function of time and after each adaptation. As a reminder, the chosen methodology consists in imposing the total inlet pressure and temperature, while manually adapting the outlet static pressure to obtain the experimental total pressure ratio at station 21A. Note that such intervention is required since losses are overestimated on coarse meshes, making it difficult to reach both the experimental total pressure ratio and the experimental mass-flow. As a result, error on the mass-flow for the used exit static pressure is large with this coarse mesh. The two successive adaptations clearly improve this mass-flow rate prediction for the same inlet total pressure ratio, indicating that losses are better captured. Note finally that with such an automatic approach, and since loss predictions change along the mesh adaptation, the outlet static pressure is the only available parameter to recover the correct total pressure ratio.

The main impact of each grid adaptation on the flow can be captured by looking at instantaneous iso-surfaces of Q-criterion as shown in Fig. 21 in the rotor domain. Clearly, the simultaneous mesh refinement in the boundary layers and in regions where dissipation occurs improves the extend, size and presence of specific turbulent flow structures in the flow topology description. While very large structures occur on the coarse mesh, very fine ones are found with "AD2". The effect may be particularly noticed on the blade near wall flow, near the shroud and the hub, as well as in mixing flow regions like the tip leakage zone, where strong kinetic energy dissipation occurs.

The resulting time and space averaged profiles are shown in Figs 22 and 23 for stations 2RD and 21A, for which the 5 hole probe measurements are accessible and added for comparison. From such profiles, one notes that downstream
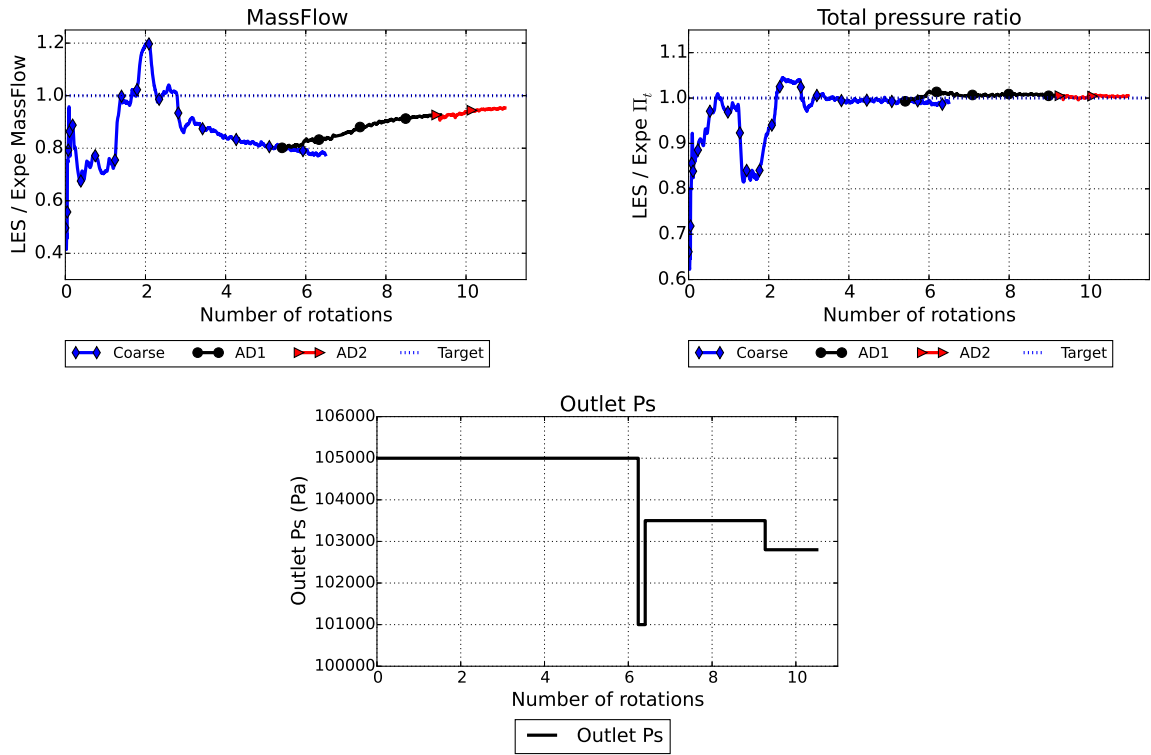
28

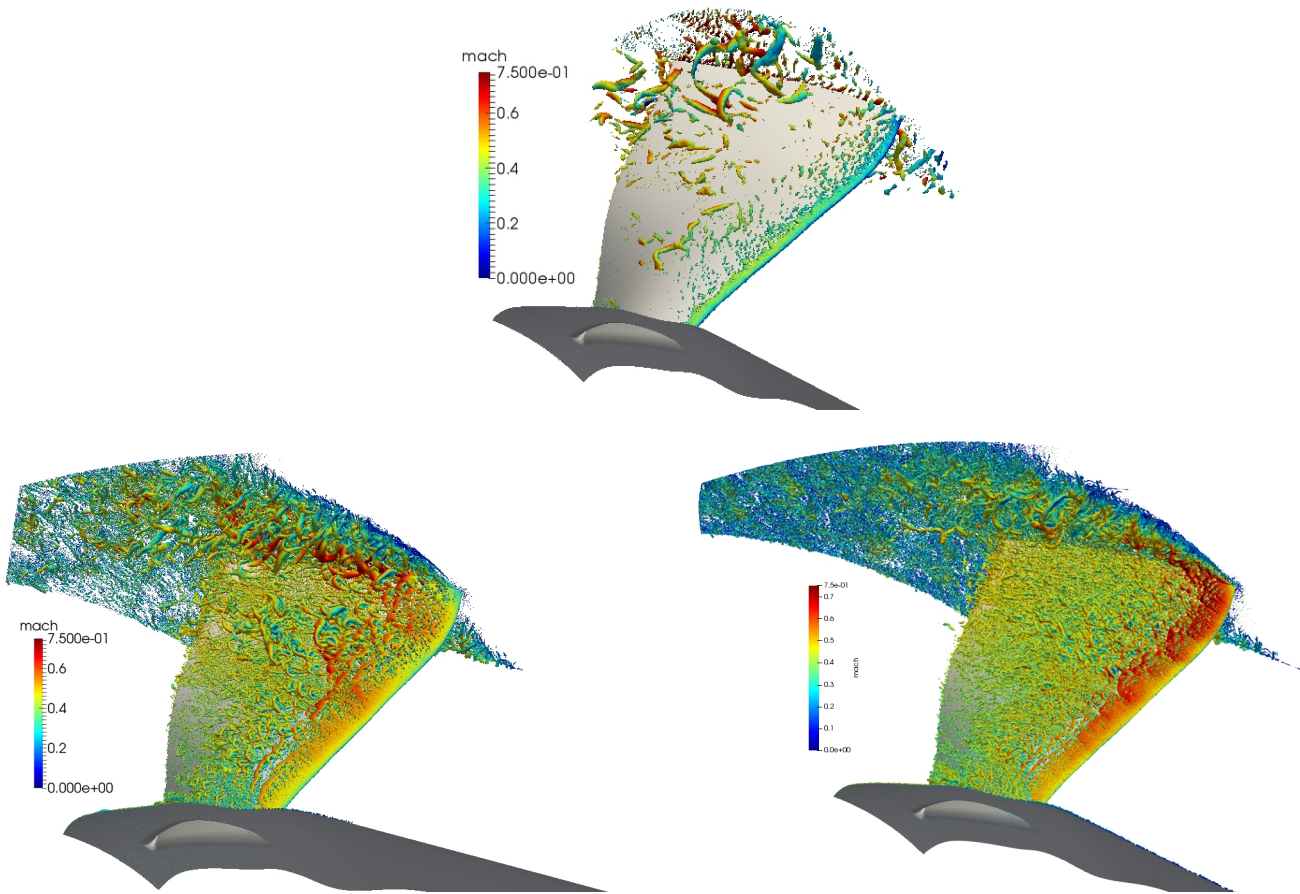Figure 20: Operating point convergence toward the target regime through the mesh adaptation process.

Figure 21: Isosurface of Q-criterion. Coarse mesh (top), "AD1" (bottom left), "AD2" (bottom right).

435 the rotor, particularly complex phenomena occur close to the casing (for high values of h/H), where the tip-leakage flow is convected and interacts with the blade and casing boundary layers. In addition to this incoming tip-leakage flow, a corner vortex occurs at the shroud in the stator domain. As shown by Figs. 22 and 23, considerable improvement is achieved by the adaptation for high values

440 of h/H. As a general conclusion, the average profiles converge to the experimental measure and a general good agreement is found for all these profiles for the last two numerical predictions.
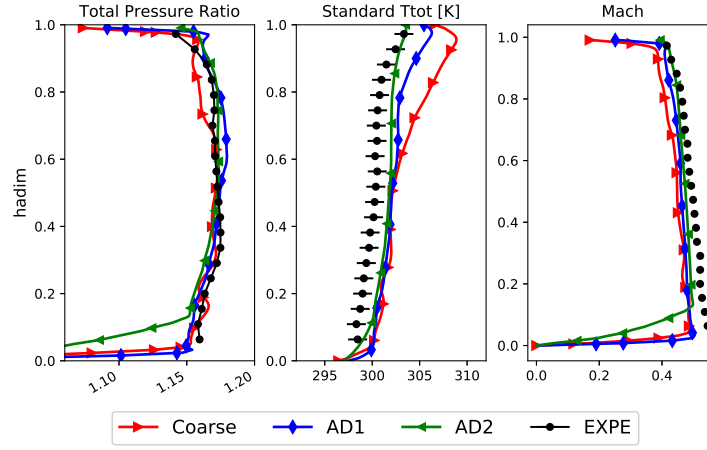

Figure 22: Average Profiles at station 2RD, between rotor and stator.

Having qualified the strategy in terms of operating condition convergence

445 and mean profiles, the present discussion is devoted to the assessement of mesh adaptation on turbulence characteristics. To do so, the unsteady velocity field is decomposed following a triple decomposition (Adamczyk [1], Hussain and Reynolds [35], Sharma et al. [56]) to separate the average velocity field $\overline{U(\mathbf{x})}$, the deterministic fluctuating part due to the periodic rotor blade passing $\tilde{u}(\mathbf{x}, t)$

450 and the stochastic fluctuation $u^{'}(\mathbf{x}, t)$. The mean field being obtained by direct
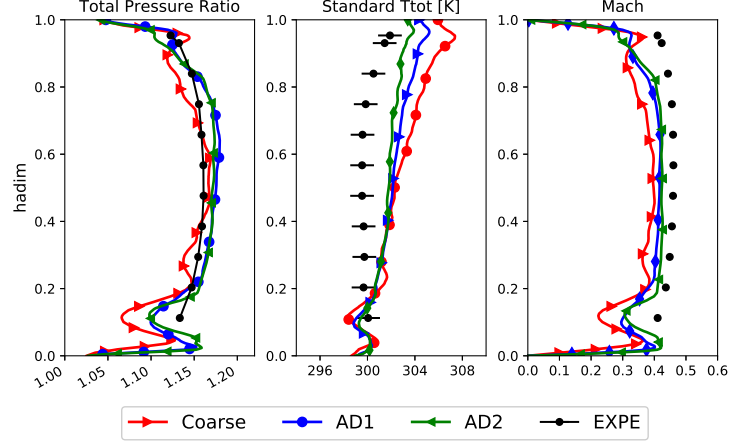
31

Figure 23: Average Profiles at station 21A, downstream of the stator.

time averaging of the predictions, a phase-averaging is applied to retrieve $\tilde{u}(\mathbf{x}, t)$ for the axial velocity component, then leading to the estimate of the remaining contribution that is $u^{'}(\mathbf{x}, t)$. Phase-averaging is performed over 9800 rotor blade passages in the experiment, while only 15 blade passages are considered in the numerical simulations for computational cost reasons.

Turbulence intensity is then characterized by the root-mean square of the stochastic fluctuation $u^{'}_{RMS}(\mathbf{x})$:

$$u^{'}_{RMS}(\mathbf{x}) = \sqrt{\frac{1}{N} \sum_{i=1}^{N} u'^2(\mathbf{x}, i)} \tag{7}$$

where N is the number of instantaneous samples. In the current study, $N = 1.080.000$ in the experiment, while $N = 600$ for the coarse and "AD1" meshes, and $N = 520$ for "AD2". The turbulence intensity is then recast as:

$$Tu(\mathbf{x}) = \frac{u^{'}_{RMS}(\mathbf{x})}{\overline{U}(\mathbf{x})} \cdot 100 \tag{8}$$

32

Maps of turbulence intensity at station 2RD, between the rotor and the stator, are presented in Fig. 24 for all cases. The coarse initial mesh is clearly unable to predict the experimental findings at the shroud (Fig.24(a)), and too high in-tensities are found. The reason for this behavior is probably related to the fact that predicted vortical structures are too large with this mesh, thus inducing ac-centuated velocity fluctuations. The prediction is significantly improved by the first adaptation (Fig.24(b)) to finally provide a very fair agreement with "AD2 (Fig. 24(d)). Similar comparisons are performed in Fig. 25 for station 21A, downstream of the stator. Once again, a poor prediction is achieved using the coarse mesh (Fig.25(a)), depicting an exaggerated wake thickness and an over-estimated turbulence intensity. A fair wake topology is predicted using "AD1" (Fig.25(b)), but this adaptation fails to accurately predict specific features (cf. previous discussion). The last adaptation improves the wake topology, with two distinguishable shear layers (Fig.25(c)), although turbulence levels still remain overpredicted. It is noteworthy that corner vortices more likely remain too large and intense with "AD2", underlining how challenging this vortex prediction can be with a wall-modeled context.

Although crucial to qualify a turbulent field, turbulent scales are rarely eval-uated in turbomachinery literature. As pointed out by Tyacke and Tucker [64], turbomachinery LES still currently needs more high-level validations and inte-gral turbulence scales are part of these potential validation metrics (Sagaut and Deck [54]). In the following, these are based on the temporal autocorrelation function $R_{uu}(\mathbf{x}, \tau)$ defined as,

$$R_{uu}(\mathbf{x}, \tau) = \frac{\overline{u'(\mathbf{x}, t) \cdot u'(\mathbf{x}, t + \tau)}}{u_{RMS}^{'\,2}(\mathbf{x})}. \tag{9}$$

To evaluate an integral turbulent time scale, its fundamental definition is used (Pope [52]):
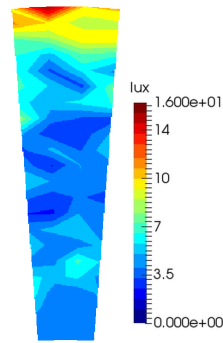
$$Lt(\mathbf{x}) = \int_{\tau=0}^{\infty} R_{uu}(\mathbf{x}, \tau) \mathrm{d}\tau \ . \tag{10}$$
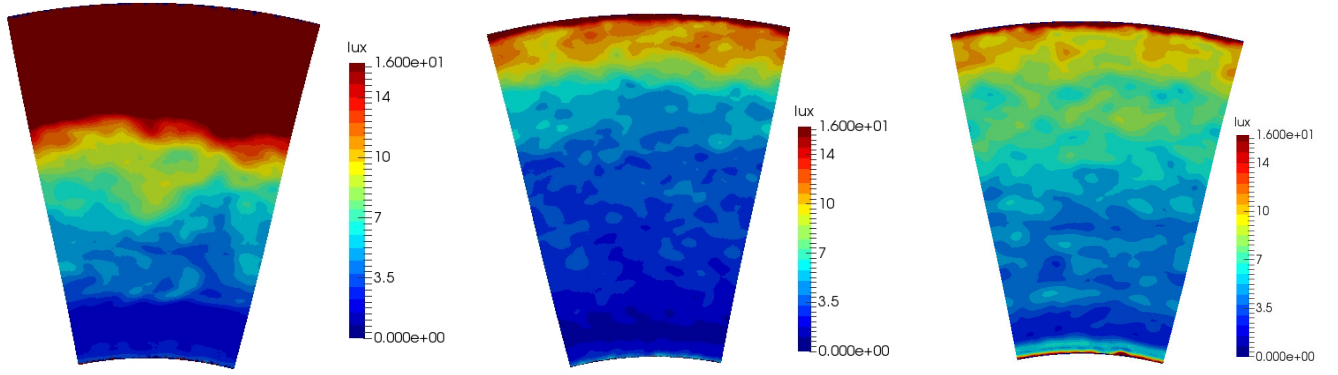
33

(a) Turbulence intensity: coarse mesh.

(b) Turbulence intensity: mesh "AD1".

(c) Turbulence intensity: mesh "AD2".

(d) Turbulence intensity: Experiment.

(e) Turbulence intensity: azimuthaly averaged radial profiles.

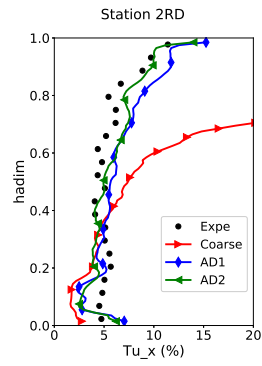Figure 24: Turbulence intensities at station 2RD.

34

(a) Turbulence intensity: coarse mesh.

(b) Turbulence intensity: mesh "AD1".
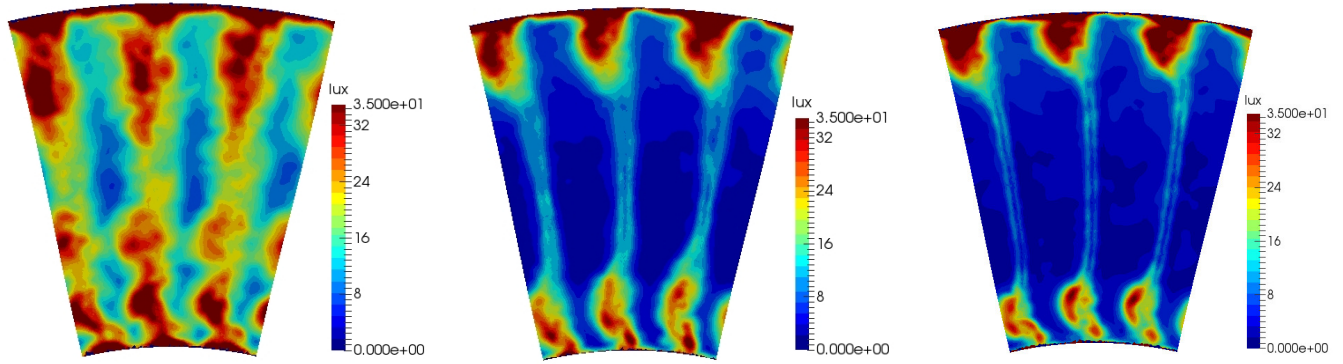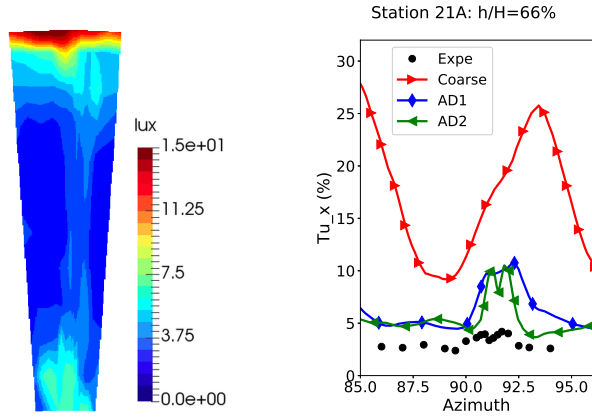

(c) Turbulence intensity: mesh "AD2".
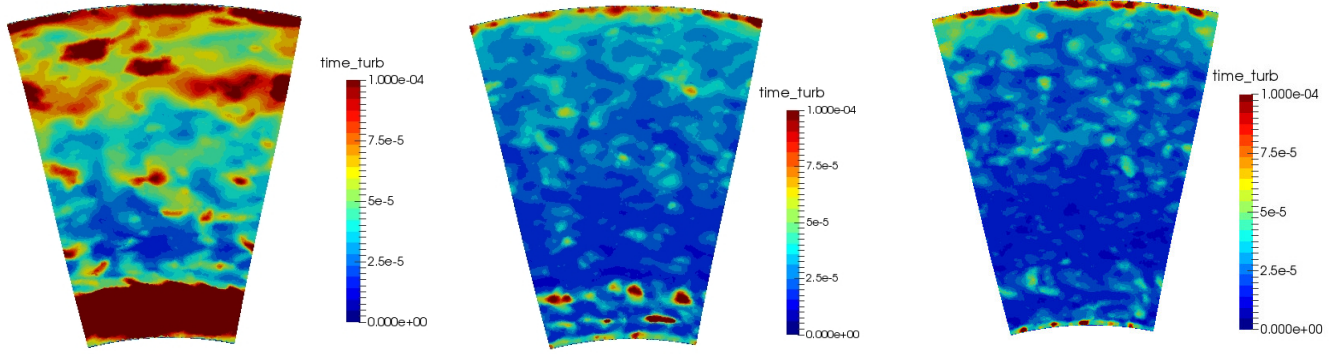

(d) Turbulence intensity: Experiment.

(e) Turbulence intensity: Azimuthal profiles at $h/H = 66\%$.

Figure 25: Turbulence intensities at station 21A.

Note that this integral may not converge for non-stationnary flows, so to circumvent this issue, R_{uu} is integrated in the following until it reaches an arbitrary threshold, noted R_{thr}, beyond which the flow is considered to be uncorrelated. In the present study, $R_{thr} = 0.25$ is considered. The exact same process for LES and for the experimental data is considered. The resulting evaluated integral turbulent time scales at station 2RD are shown in Fig. 26. For the coarse mesh prediction and in agreement with the previous findings, overestimated values are found (Fig.26(a)), particularly close to the hub. Very good agreement with the experimental integral time scales are recovered as soon as the mesh adaptation is introduced: Figs.26(b) to 26(d). The same comparison for station 21A is provided on Fig. 27, and for which a fair estimate is found even with the coarse mesh, Fig.27(a), if compared to the experiment, Fig.27(d). However, as previously discussed, wake thickness and more generally mean fields are mispredicted on this mesh. Finally, a very good agreement is found for the adapted meshes "AD1" and "AD2" which at the same time really improve associated mean fields as well as the stator wake thickness.

Conclusions

A mesh adaptation strategy for unstructured, wall-modeled, complex turbomachinery LES configurations is proposed and qualified as a first attempt to ease the use of LES in an industrial design phase. The adaptation is based on two criteria, simultaneously accounting for the normalized wall distance y^+ and the loss in kinetic energy. In order to evaluate the impact of this automatic strategy, tests are performed first on a highly loaded cascade exhibiting a recirculation bubble on its pressure side and a shock region on its suction side. Such typical turbomachinery flow features are known as challenging situations for numerical predictions and the objective is to qualify the proposed strategy knowing that a wall-modeled approach shows limits for such a case. Despite these limitations, adaptation is seen to capture first order flow characteristics, i.e. pressure distribution and recirculation bubble.

(a) Turbulence time scale: coarse mesh.

(b) Turbulence time scale: mesh "AD1".

(c) Turbulence time scale: mesh "AD2".
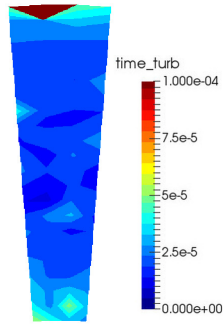
(d) Turbulence time scale: Experiment.

(e) Turbulence time scale: azimuthaly averaged radial profiles.

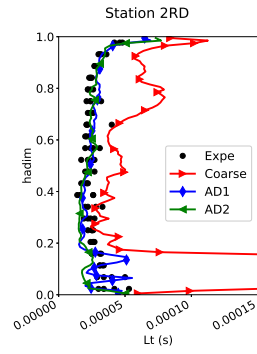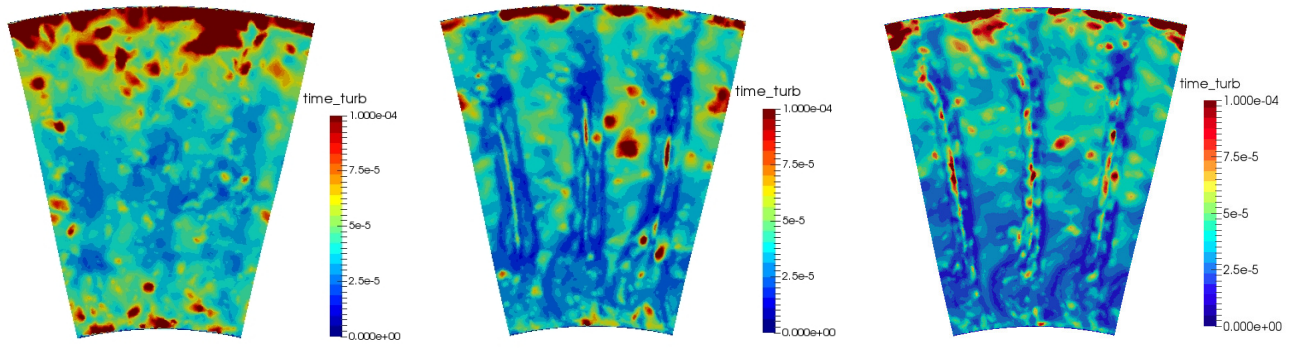Figure 26: Turbulence integral scales at station 2RD.

(a) Turbulence time scale: coarse mesh.

(b) Turbulence time scale: mesh "AD1".

(c) Turbulence time scale: mesh "AD2".
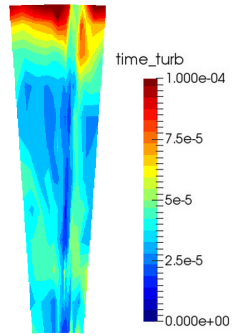
(d) Turbulence time scale: Experiment.

Figure 27: Turbulence integral scales at station 21A.

The proposed methodology is then tested on a second configuration: a real turbofan stage. For this problem, the modeling coupled to the adaptation scheme leads the numerical operating point to converge towards the experimental one, as well as the averaged azimuthal mean profiles. Insight on turbulence characteristics obtained from the prediction is then compared to hot-wire anemometry measurements. Very fair results are found regarding both turbulence intensities and turbulence integral time scales as soon as mesh adaptation is introduced. Specific flow features are however missing, like the stator corner vortices which remain mispredicted even with a second mesh adaptation step. Despite this challenging issue attributed to the law of the wall modeling, a general confidence in the proposed method is demonstrated even for a complex configuration.

Acknowledgments

References

[1] Adamczyk, J. J. (1985). Model equation for simulating flows in multistage turbomachinery. In *ASME, International Gas Turbine Conference and Exhibit*. Houston, Texas volume 85-GT226.

[2] Afzal, N. (1996). IUTAM Symposium on Asymptotic Methods for Turbulent Shear Flows at High Reynolds Numbers. In *IUTAM Smposium on*

39

545   *Asymptotic Methods for Turbulent Shear Flows at High Reynolds Numbers*
       (pp. 94–117). volume 37.

[3] Alauzet, F., Frey, P. J., George, P. L., & Mohammadi, B. (2007). 3D
    transient fixed point mesh adaptation for time-dependent problems: Ap-
    plication to CFD simulations. *Journal of Computational Physics*, *222*,
550   592–623.

[4] Ali, Z., Dhanasekaran, P. C., Tucker, P. G., Watson, R., & Shahpar, S.
    (2017). Optimal multi-block mesh generation for CFD. *International Jour-
    nal of Computational Fluid Dynamics*, *31*, 195–213.

[5] Ali, Z., & Tucker, P. G. (2014). Multiblock structured mesh generation for
555   turbomachinery flows. In *Proceedings of the 22nd International Meshing
    Roundtable* (pp. 165–182). Orlando, Florida.

[6] Amone, A., Ennio, C., & Marconcini, M. (1997). Grid dependency study
    for the NASA rotor 37 compressor blade. In *International Gas Turbine &
    Aerospace Congress & Exhibition*. Orlando, Florida.

560 [7] Antepara, O., Lehmkuhl, O., Borrell, R., Chiva, J., & Oliva, A. (2015).
    Parallel adaptive mesh refinement for large-eddy simulations of turbulent
    flows. *Computers and Fluids*, *110*, 48–61.

[8] Arts, T., Lambert de Rouvroit, M., & Rutherford, A. (1990). *Aero-thermal
    investigation of a highly loaded transonic linear turbine vane cascade*. Tech-
565   nical Report September Von Karman Institute for Fluid Dynamics.

[9] Bae, H. J., Lozano-Durán, A., Bose, S. T., & Moin, P. (2019). Dynamic
    slip wall model for large-eddy simulation. *J. Fluid Mech.*, *859*, 400–432.

[10] Benard, P., Balarac, G., Moureau, V., Dobrzynski, C., Lartigue, G., &
    D'Angelo, Y. (2015). Mesh adaptation for large-eddy simulations in com-
570   plex geometries. *International Journal for Numerical Methods in Fluids*,
    81, 719–740.

[11] Bose, S. T., & Park, G. I. (2018). Wall-Modeled Large-Eddy Simulation for Complex Turbulent Flows. *Annual Review of Fluid Mechanics*, *50*, 535–561.

[12] Catchirayer, M., Boussuge, J.-F., Sagaut, P., Montagnac, M., Papadogiannis, D., & Garnaud, X. (2018). Extended integral wall-model for large-eddy simulations of compressible wall-bounded turbulent flows. *Physics of Fluids*, *30*, 1–20.

[13] Colin, O., & Rudgyard, M. (2000). Development of High-Order Taylor-Galerkin Schemes for LES. *Journal of Computational Physics*, *162*, 338–371.

[14] Dapogny, C., Dobrzynski, C., & Frey, P. (2014). Three-dimensional adaptive domain remeshing, implicit domain meshing, and applications to free and moving boundary problems. *Journal of Computational Physics*, *262*, 358–378.

[15] Daviller, G., Brebion, M., Xavier, P., Staffelbach, G., & Poinsot, T. (2017). A mesh adaptation strategy to predict pressure losses in LES of swirled flows. *Flow, Turbulence and Combustion*, *99*, 93–118.

[16] Dawes, W. N. (1992). The Simulation of Three- Dimensional Viscous Flow in Turbomachinery Geometries Using a Solution-Adaptive Unstructured Mesh Methodology. *Trans. ASME*, *114*.

[17] Deardorff, J. W. (1970). A numerical study of three-dimensional turbulent channel flow at large Reynolds numbers. *Journal of Fluid Mechanics*, *41*, 453–480.

[18] Denton, J. D. (1993). Loss Mechanisms in Turbomachines. *J. Turbomach.*, *115*, 621–656.

[19] Denton, J. D. (1997). Lessons from Rotor 37. *Journal of Thermal Science*, *6*, 1–13.

[20] Dufour, G., Gourdain, N., Duchaine, F., Vermorel, O., & Poinsot, T. (2009). Numerical Investigations in Turbomachinery : A State of the Art Large Eddy Simulation Applications. In *VKI Lecture Series* (pp. 21–25). Sint-Genesius-Rode, Belgium: Von Karman Institute.

[21] Duprat, C., Balarac, G., Métais, O., Congedo, P. M., & Brugière, O. (2011). A wall-layer model for large-eddy simulations of turbulent flows with/out pressure gradient. *Physics of Fluids*, *23*.

[22] Fidkowski, K. J., & Darmofal, D. L. (2011). Review of Output-Based Error Estimation and Mesh Adaptation in Computational Fluid Dynamics. *AIAA Journal*, *49*, 673–694.

[23] Frazza, L., Alauzet, F., & Loseille, A. (2018). Mesh adaptation strategies using wall functions and low-Reynolds models. In *2018 Fluid Dynamics Conference* (pp. 1–14). Atlanta, Georgia, USA.

[24] Frazza, L., Loseille, A., & Alauzet, F. (2017). Anisotropic mesh adaptation for turbomachinery applications. In *23rd AIAA Computational Fluid Dynamics Conference, 2017*.

[25] Frey, P. J., & Alauzet, F. (2005). Anisotropic mesh adaptation for CFD computations. *Computer Methods in Applied Mechanics and Engineering*, *194*, 5068–5082.

[26] García Rosa, N., Dufour, G., Barènes, R., & Lavergne, G. (2015). Experimental Analysis of the Global Performance and the Flow Through a High-Bypass Turbofan in Windmilling Conditions. *Journal of Turbomachinery*, *137*, 051001.

[27] Giles, M. B., & Pierce, N. A. (2003). Adjoint Error Correction for Integral Outputs. In *Lecture Notes in Computational Science and Engineering: Error Estimation and Adaptive Discretization Methods in Computational Fluid Dynamics* (pp. 47–95). Berlin: Springer.

[28] Gomes, R. A., & Niehuis, R. (2010). High Loading and Vortex Generators. In *ASME Turbo Expo 2010: Power for Land, Sea and Air*. Glasgow, UK.

[29] Gou, J., Su, X., & Yuan, X. (2018). Adaptive mesh refinement method-based large eddy simulation for the flow over circular cylinder at ReD= 3900. *International Journal of Computational Fluid Dynamics*, *32*, 1–18.

[30] Gou, J., Yuan, X., & Su, X. (2017). Adaptive mesh refinement method based investigation of the interaction between shock wave, boundary layer, and tip vortex in a transonic compressor. *Proceedings of the Institution of Mechanical Engineers, Part G: Journal of Aerospace Engineering*, *232*, 694–715.

[31] Gourdain, N., Gicquel, L., Montagnac, M., Vermorel, O., Gazaix, M., Staffelbach, G., Garcia, M., Boussuge, J.-F., & Poinsot, T. (2009). High performance parallel computing of flows in complex geometries: I. Methods. *Computational Science & Discovery*, *2*, 015003.

[32] Gourdain, N., Sicot, F., Duchaine, F., & Gicquel, L. (2014). Large eddy simulation of flows in industrial compressors: a path from 2015 to 2035. *Philosophical Transactions of the Royal Society A: Mathematical, Physical and Engineering Sciences*, *372*, 20130323–20130323.

[33] Harnieh, M., Gicquel, L., & Duchaine, F. (2017). Sensitivity of Large Eddy Simulations To Inflow Condition and. In *Proceedings of the ASME Turbo Expo 2017: Turbomachinery Technical Conference and Exposition*. Charlotte, NC, USA.

[34] Harnieh, M., Gicquel, L., & Duchaine, F. (2018). Large Eddy Simulations of a Highly Loaded Transonic Blade With Separated Flow. In *ASME Turbo Expo 2018*. Oslo, Norway.

[35] Hussain, A. K. M. F., & Reynolds, W. C. (1970). The mechanics of an organized wave in turbulent shear flow. Part 2. Experimental results. *Journal of Fluid Mechanics*, *54*, 241.

43

[36] Jones, W. T., Nielsen, E. J., & Park, M. A. (2006). Validation of 3D Adjoint Based Error Estimation and Mesh Adaptation for Sonic Boom Reduction. *AIAA paper*, *2006-1150*.

[37] Kawai, S., & Larsson, J. (2013). Dynamic non-equilibrium wall-modeling for large eddy simulation at high Reynolds numbers. *Physics of Fluids*, *25*.

[38] de Laborderie, J., Duchaine, F., Gicquel, L., Vermorel, O., Wang, G., & Moreau, S. (2018). Numerical analysis of a high-order unstructured overset grid method for compressible LES of turbomachinery. *Journal of Computational Physics*, *363*, 371–398.

[39] Larsson, J., Kawa Soshi, Bodart, J., & Bermejo, I. (2016). Large eddy simulation with modeled wall-stress: recent progress and future directions. *Mechanical Engineering Reviews*, *3*, 15–00418–15–00418.

[40] Larsson, J., & Wang, Q. (2014). The prospect of using large eddy and detached eddy simulations in engineering design, and the research required to get there. *Philosophical Transactions of the Royal Society A: Mathematical, Physical and Engineering Sciences*, *372*, 1–15.

[41] Lax, P., & Wendroff, B. (1960). Systems of conservation laws. *Commun. Pure Appl. Math*, *13*, 217–237.

[42] Müller, J.-d., & Giles, M. B. (2001). Solution Adaptive Mesh Refinement Using Adjoint Error Analysis. In *15th Computational Fluid Dynamics Conference*. Anaheim, California.

[43] Nemec, M., & Aftosmis, M. J. (2007). Adjoint error estimation and adaptative refinement for embedded-boundary cartesian meshes. In *18th AIAA Computational Fluid Dynamics Conference* June. Miami, FL, USA.

[44] Odier, N., Poinsot, T., Duchaine, F., Gicquel, L., & Moreau, S. (2019). Inlet and outlet characteristics boundary conditions for large eddy simulations of turbomachinery. In *ASME Turbo Expo 2019: Turbomachinery Technical Conference & Exposition*. Phoenix, AZ, USA.

[45] Odier, N., Sanjosé, M., Gicquel, L., Poinsot, T., Moreau, S., & Duchaine, F. (2019). A characteristic inlet boundary condition for compressible, turbulent, multispecies turbomachinery flows. *Computers & Fluids*, *178*, 41–55.

[46] Park, G. I., & Moin, P. (2014). An improved dynamic non-equilibrium wall-model for large eddy simulation. *Physics of Fluids*, *26*, 0–21.

[47] Peter, J., Nguyen-Dinh, M., & Trontin, P. (2012). Goal oriented mesh adaptation using total derivative of aerodynamic functions with respect to mesh coordinates - With applications to Euler flows. *Computers and Fluids*, *66*, 194–214.

[48] Pierce, N. A., & Giles, M. B. (2004). Adjoint and defect error bounding and correction for functional estimates. *Journal of Computational Physics*, *200*, 769–794.

[49] Piomelli, U. (2008). Wall-layer models for large-eddy simulations. *Progress in Aerospace Sciences*, *44*, 437–446.

[50] Piomelli, U., & Balaras, E. (2002). Wall-Layer models for Large-Eddy Simulations. *Annu. Rev. Fluid Mech.*, *34*, 349–374.

[51] Poinsot, T. J., & Lele, S. K. (1992). Boundary conditions for direct simulations of compressible viscous flows. *Journal of Computational Physics*, *101*, 104–129.

[52] Pope, S. (2000). *Turbulent Flows*. Cambridge University Press.

[53] Rai, M., & Madavan, N. K. (1990). Multi-Airfoil Navier-Stokes Simulations of Turbine Rotor-Stator Interaction. *Journal of Turbomachinery*, *112*, 377–384.

[54] Sagaut, P., & Deck, S. (2009). Large eddy simulation for aerodynamics: status and perspectives. *Philosophical Transactions of the Royal Society A: Mathematical, Physical and Engineering Sciences*, *367*, 2849–2860.

[55] Schønfeld, T., & Rudgyard, M. (1999). Steady and unsteady flows simulations using the hybrid flow solver avbp. *AIAA Journal*, *37*, 1378–1385.

[56] Sharma, O. P., Butlert, T. L., Joslyn, H., & Drings, R. (1985). Three-Dimensional Unsteady Flow in an Axial Flow Turbine. *Journal of Propulsion and Power*, *1*, 29–38.

[57] Spalart, P. R. (2009). Detached-Eddy Simulation. *Annual Review of Fluid Mechanics*, *41*, 181–202.

[58] Spalart, P. R., Jou, W., Strelets, M. K., & Allmaras, S. (1997). Comments on the feasibility of LES for wings, and on a hybrid RANS/LES approach. In *Proceedings of the first AFOSR International Conference on DNS/LES*. Ruston, Louisiana, USA.

[59] Thacker, A., García Rosa, N., & Dufour, G. (2017). Experimental analysis of the unsteady, turbulent flow through the fan stage of a high-bypass turbofan in windmilling conditions. In *European Turbomachinery Conference*. Stockholm, Sweden.

[60] Toosi, S., & Larsson, J. (2017). Anisotropic grid-adaptation in large eddy simulations. *Computers and Fluids*, *156*, 146–161.

[61] Tucker, P. G. (2011). Progress in Aerospace Sciences Computation of unsteady turbomachinery flows : Part 1 Progress and challenges. *Progress in Aerospace Sciences*, *47*, 522–545.

[62] Tucker, P. G. (2011). Progress in Aerospace Sciences Computation of unsteady turbomachinery flows : Part 2 LES and hybrids. *Progress in Aerospace Sciences*, *47*, 546–569.

[63] Tucker, P. G. (2013). *Unsteady Computational Fluid Dynamics in Aeronautics*. Springer.

[64] Tyacke, J. C., & Tucker, P. G. (2015). Future use of Large Eddy Simulation in aeroengines. *Journal of Turbomachinery*, *137*, GT2014–25434.

₇₃₅ [65] Venditti, D. A., & Darmofal, D. L. (2002). Grid adaptation for functional outputs: Application to two-dimensional inviscid flows. *Journal of Computational Physics*, *176*, 40–69.

[66] Vivarelli, G., Qin, N., & Shahpar, S. (2017). Combined Hessian and Adjoint Error-Based Anisotropic Mesh Adaptation for Turbomachinery Flows. In ₇₄₀ *55th AIAA Aerospace Sciences Meeting* January. Grapevine, Texas, USA.

[67] Vivarelli, G., Qin, N., Shahpar, S., & Radford, D. (2018). Efficient adjoint-based mesh adaptation applied to turbo-machinery flows. In *Proceedings of the ASME Turbo Expo*. Oslo, Norway volume 2C-2018.

[68] Wang, G., Duchaine, F., Papadogiannis, D., Duran, I., Moreau, S., & ₇₄₅ Gicquel, L. (2014). An overset grid method for large eddy simulation of turbomachinery stages. *Journal of Computational Physics*, *274*, 333–355.

[69] Yang, X. I., Park, G. I., & Moin, P. (2017). Log-layer mismatch and modeling of the fluctuating wall stress in wall-modeled large-eddy simulations. *Physical Review Fluids*, *2*, 1–13.

₇₅₀ [70] Yang, X. I., Sadique, J., Mittal, R., & Meneveau, C. (2015). Integral wall model for large eddy simulations of wall-bounded turbulent flows. *Physics of Fluids*, *27*, 1–32.